ALEPH 93-149
PHYSIC 93-129
B. Bloch-Devaux et al.
8.9.1993

The 1992 SiCAL luminosity analysis

B. Bloch-Devaux, E. Lançon, J. Rander, J.P. Schuller, B. Vallage (Saclay), J. Boudreau, R. Miquel, J. Perlas (CERN), R. Fantechi, E. Mannelli, A. Valassi (Pisa)

Abstract

The new silicon-tungsten luminosity calorimeter (SiCAL) was installed in ALEPH in September, 1992. The absolute luminosity is measured with an estimated precision of 0.15 % (experimental) and 0.25 % (theoretical) for this two-month data taking period. In this note we discuss the detector, the luminosity event selection and the various contributions to the 1992 luminosity error.

1 Introduction

The absolute luminosity measurement is essential to the determination of the Z parameters, and in particular to the measurement of the peak hadronic cross-section σ^0_{had}. The determination of the number of light neutrino species is limited by the absolute luminosity systematic error. The SiCAL was designed to measure the luminosity with an experimental precision better than 0.2 % and reduce the luminosity statistical error (with respect to LCAL) by roughly $\sqrt{4.7}$ [1, 2]. The detector was installed in September 1992 and collected data for two months, during which an integrated luminosity of 8749 $\pm$ 28 nb^{-1} was accumulated. In the following sections we discuss the various tests and cross-checks used to evaluate systematic errors on the 1992 SiCAL luminosity. This analysis of the first running with SiCAL has profited from the earlier LCAL and SATR measurements of absolute luminosity in ALEPH [3].

2 Detector

The SiCAL luminosity detector is a silicon-tungsten sampling electromagnetic calorimeter, 23.4 Xo in depth. Total energy and position of showers are measured with 5.225 mm wide radial pads (x 11.25° in ϕ). Full information on the shower development is available since all pads are readout individually. These energy deposits are reconstructed off-line into clusters upon which the luminosity measurement is based. A detailed technical description of the SiCAL luminosity monitor is in preparation [4], so only details directly revelant to the luminosity analysis will be presented here.

The SiCAL detector characteristics are summarized in Table 1. The detector consists of two homogenous cylindrical sampling calorimeters which surround the beam pipe at roughly $\pm$250 cm from the interaction point. The calorimeters have inner and outer radii of 6.1 and 14.5 cm and an active volume subtending an angular region between 24 and 58 mrads. Twelve layers of tungsten alternate with layers of silicon pad detectors, each layer being segmented into 16 cylindrical pad rows in radius, and 32 sectors in azimuth, for a total of 12288 pads. Successive layers are rotated by 3.75°. This staggered construction guarantees that there is no aligned crack between assembled half modules.

The basic detector element is the 300 μm thick silicon detector: two ϕ-sectors divided into 16 radial pads (all silicon detectors are identical, there is no "projective" pad geometry with increasing depth). A minimum ionizing particle deposits 3.8 fC in a single pad, and a 45 GeV electron deposits about 1.7 pC at the shower maximum. This signal is integrated in a charge sensitive amplifier located near the silicon detector. The amplifier, AMPLEX-SiCAL [5], reads 16 input channels (corresponding to the 16 radial bins of one ϕ-sector) which are preamplified, shaped and "held", and then multiplexed into a single output for readout. The AMPLEX-SiCAL chip has internal calibration circuitry consisting of CMOS switches and calibrated capacitors connected to each input. This allows individual channel calibration to $\leq$ 1 %. An "analog-sum" (16 channel average) is produced for triggering SiCAL.

Description:	
– Tungsten layers	12
– Silicon thickness	300μm
– Total silicon surface	1.3 m^2
– Sampling	1.95 Xo
– ϕ divisions	32
– Radial divisions	16
– Total number of pads	12288
Dimensions:	
– Inner radius (Si-pad)	6.10 cm
– Outer radius (Si-pad)	14.45 cm
– Length	13.00 cm
– Z position of 1st Si-layer	250.32 cm
Acceptance:	
– θ_{min}	24 mrad
– θ_{max}	58 mrad
Performance:	
– Cell to cell uniformity	0.5%
– Noise per channel	$\simeq$ 0.7 fC
– Pads per 45 GeV cluster	91 $\pm$ 10 pads
– Energy resolution	$34\%/\sqrt{E}$
– Radial position	0.020 cm
– ϕ position	3.8 mrad

Table 1: *SiCAL parameters.*

The analog-sum and the 16 channel analog signals are sent sequentially both to the readout and to the trigger. The readout uses the same Fastbus multiplexed analog to digital converters (MUX-ADC) as used for ALEPH-ECAL. As a result, the 12 SiCAL layers are grouped during readout into 4 successive triplet "stacks" in agreement with the ECAL readout structure. Zero-suppression is performed at the MUX-ADC level by suppressing the readout of triplets of pads where the largest individual signal is less than 4 ADC counts ($<$ 20 MeV). The multiplexing and readout synchronization is controlled via a programmable sequencer.

The dense readout of the calorimeter stack (every hit pad) gives a detailed measurement of the shower profile which permits the luminosity fiducial selection to be based upon partial energy sums (narrow radial strips summed over two layers).

The trigger electronics is based upon 7-bit flash-ADC's and programmable gate arrays. The analog-sum from the AMPLEX-SiCAL chip defines the primary trigger element as a single 11.25° ϕ-sector from which trigger "roads" are composed (described in section 3). Furthermore, the readout of every layer allows two independent triggers for each calorimeter (based on "odd" or "even" layers) which are used to cross-check the trigger-efficiency.

2.1 Detector mechanics

The internal precision of the detector mechanical design has been discussed in detail elsewhere [7]; in what follows we will review and update those elements which are essential to the present measurement. The mechanical precision is summarized in Table 2.

2.1.1 Silicon pad and G10 support ring measurements

The relative positioning of the pad detectors is of crucial importance to the luminosity measurement. Photolithography of each silicon wafer using a mask assures the reproducibility of the pad geometry ($\pm 2\mu$m) [6]. The silicon

detectors are glued under a microscope onto thin ceramic supports to form ceramic-silicon-kapton foil (CESIKA) sub-assemblies. Following the gluing operation, a fraction of the CESIKA sub-assemblies were checked for radial position precision: the distance D between the center of the separation between radial pad rows 14-15 and the ceramic support's positioning hole was measured, $\sigma_D = 9\mu$m, shown in Figure 1.

The CESIKA units in turn are positioned onto "G10" (ME730) support half-rings with high-precision pins in order to form a sampling layer. The positioning holes in pairs of "G10" support half-rings were measured (before their division) using an industrial computerized scanning table [8], maintained at 20° C. This temperature was chosen to be close to the ALEPH operating conditions, however, it did not correspond to the final SiCAL operating temperature and is responsable for some loss in precision (see the next sub-section). The reproducibility of measurements was found to be within 5 μm ($\sigma_x = 4\mu$m, $\sigma_y = 2\mu$m) for the positioning pin holes. Although the values agreed from board to board within 17 μm in x and 23 μm in y, we chose to enter them into the database. The ϕ dispersion σ_ϕ between "expected" and measured ϕ was found to be 0.010°, which is far smaller than required for the luminosity measurement. As a result only the radial positions are presently determined from the database values.

The "G10" half-rings are stacked onto rods supported by the calorimeter case. The tolerance of the fit between support rod and the hole in the "G10" gives a radial uncertainty of 10 μm, which is further reduced by summing over two layers for the fiducial cut.

2.1.2 Half-module relative positions

The relative positions of each of the half-module pairs are measured continuously using 4 infrared light emitting diodes (LED) mounted on one half-module, read by segmented photodiodes mounted on the adjacent half-module, shown in Figure 2. Currents in the four quarters (a,b,c,d) of each photodiode are converted into two analog signals:

$$x = \frac{(a+d)-(b+c)}{a+b+c+d} \tag{1}$$

$$y = \frac{(a+b)-(c+d)}{a+b+c+d} \tag{2}$$

which are readout via the slow-control system. The measurement precision of each group, including stability of the electronics is 5 μm in x and y. Measurements of the half-module separations during the shut-downs permitted an absolute calibration of these distances to 8 μm.

Figures 3 shows the stability of the LED x-measurements over the data collection period in 1992. The maximum drift is less than 8 μm. As a result, the 1992 analysis used only the averaged positions from these measurements.

2.1.3 Thermal stability measurements

The dimensional stability of the "G10" support plates is critical to the radial precision. The detector is both water-cooled ($T_{H2O} = 21.6°$ C.) and air-cooled in order to maintain an operating temperature which is both stable and as close as possible to the ALEPH temperature. The internal temperature of SiCAL is verified with probes which are readout via the slow-control system. Figure 4 shows the thermal stability ($\sigma_T \leq 0.3°$ C.) over the data-taking

(1) Silicon pad relative to CESIKA alignment hole	9 μm
(2) Alignment pin, CESIKA and G10 hole tolerances	5 μm
(3) Alignment hole position on G10 support	5 μm
(4) G10 support thermal distortion effects	16 μm
(5) Support rod and hole tolerance	10 μm
(6) Support rod hole position on G10 support	5 μm
(7) Half-module separation LED precisions	5 μm
(8) LED sensors calibration uncertainty	8 μm
Total "effective" radial uncertainty	18 μm

Table 2: *Summary of SiCAL mechanical uncertainties. The total uncertainty is evaluated assuming that the errors 1, 2 and 3 are reduced by the 16 CESIKA units per layer, that errors 5 and 6 concern two layers, and that the final error is further reduced for the side-A and side-B selections, except for thermal effects which are certainly coherent.*

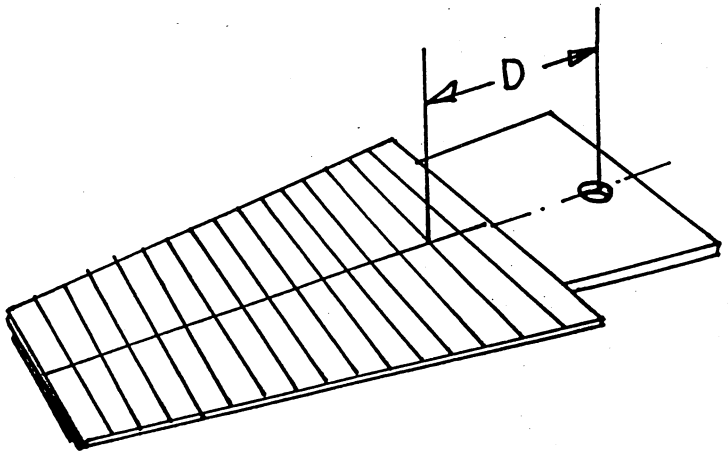

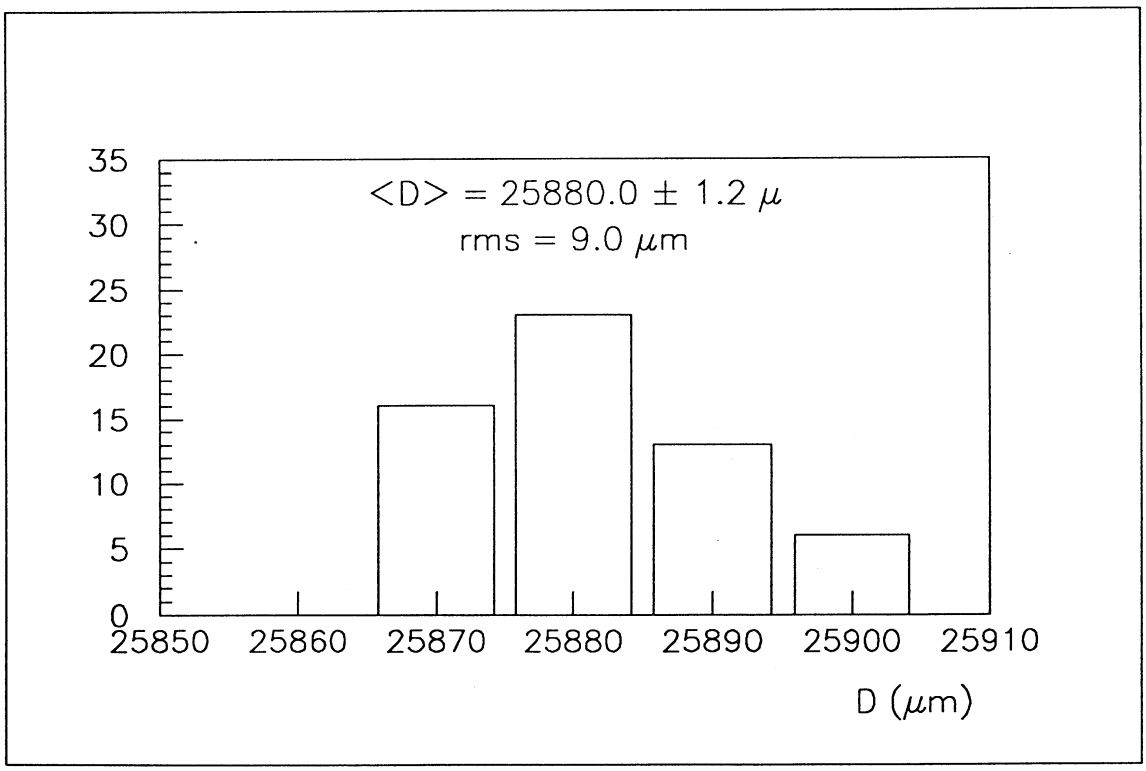

Figure 1: *Measurements of a sample of ceramic-silicon-kapton foil sub-assemblies: the radial distance between the positioning pin hole and the pad 14-15 boundary (illustrated above) is consistent with the measurement resolution.*

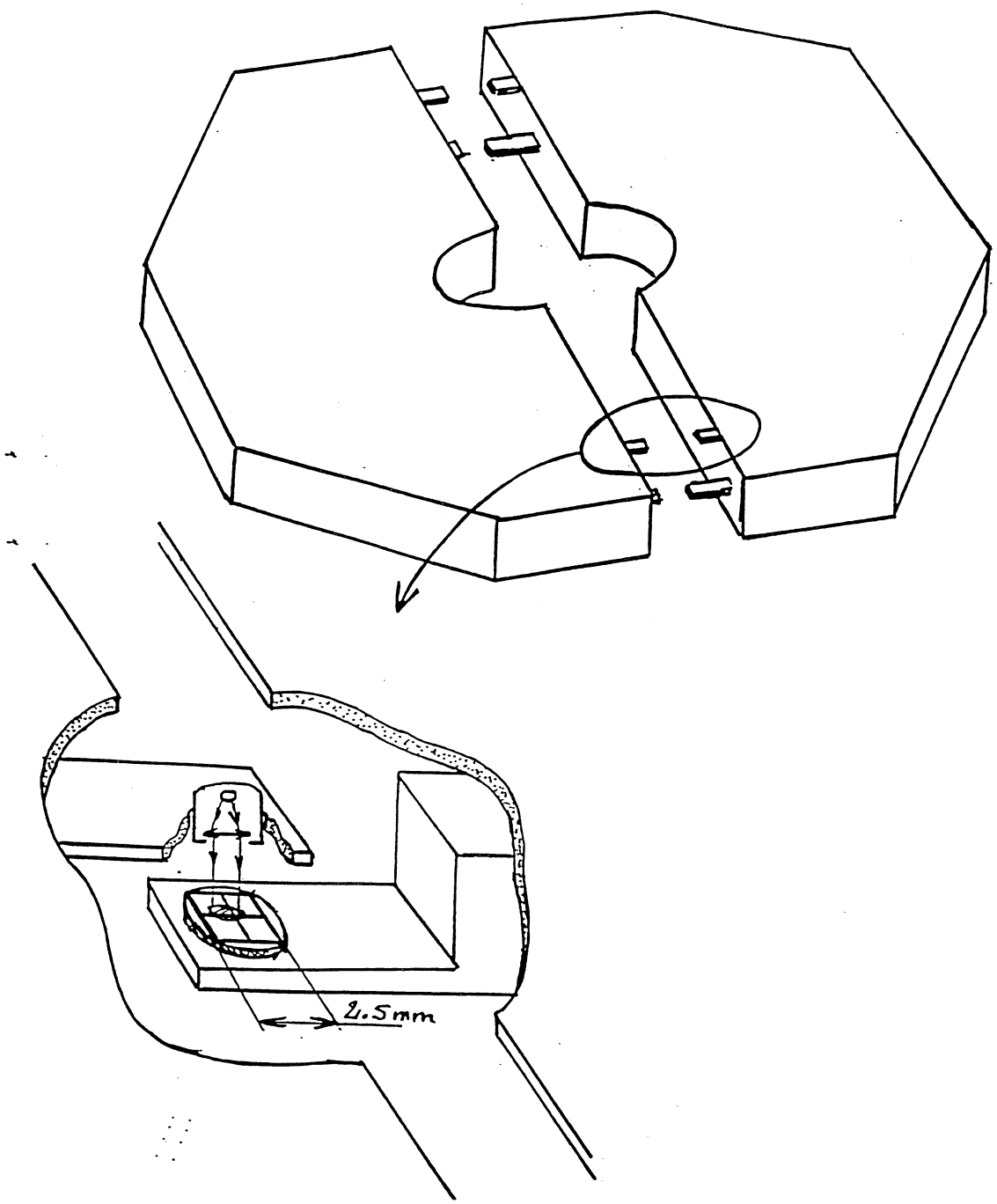

Figure 2: *Arrangement of the groups of light emitting diodes and segmented photodiode receivers on a pair of SiCAL half-modules. Measurement precision of 5 μm is obtained in x and y.*

period. Although interruptions of the low voltage supplies (eg. shutdowns) rapidly lowers the detector's average temperature, this returns to its "plateau" value in roughly 2 to 3 hours of operation. Care was taken during ALEPH data-taking to maintain SiCAL low voltages.

The average operating temperature of SiCAL $< T^{\circ} >$ was $\simeq$ 25° C, whereas the measurements of the CESIKA alignment holes described above (section 2.1.1) were performed at 20° C. The effect on the radial measurements can be estimated as follows: the material used for the "G10" boards (MEV 730) has a linear thermal expansion coefficient α_T of 1.3×10^{-5}, using the distance between the support and the center of the plate, 24.5 cm, yields 16 μm for 5° C. difference. Rather than correct for this amount, the present analysis assumes, conservatively, that this represents the systematic uncertainty of the support plate radial dimensions. (It is forseen to perform new measurements at 25° C. to remove part of this error for the 1993/1994 analysis).

3 Trigger Design

The SiCAL trigger is designed for 100% efficiency for Bhabha scattering events within the defined acceptance. Independent checks of the trigger efficiency have been built into the trigger system. In this section we will describe briefly how the trigger works and how its performance is verified.

The trigger is built from ϕ sectors corresponding to the fast-or sums available from individual AMPLEXes. Two superimposed trigger ϕ-subdivisions are made for each endcap, both consisting of eight 45° trigger segments, one offset in ϕ by 45°/2 with respect to the other. The angular width was chosen such that an electromagnetic shower would be fully contained in at least one segment of either "road 1" or "road 2" sub-division. Within each trigger segment energies are summed independently over the odd and even planes, and compared against a set of thresholds. The odd/even triggers permit independent efficiency measurement with the same ϕ coverage. The Bhabha coincidence trigger requires a large energy deposit in one endcap together with a less restrictive energy requirement in the other. This trigger is called $A_{high} \bullet B_{low} + A_{low} \bullet B_{high}$. Typically the high and low thresholds were 24 GeV and 12 GeV in 1992 (the trigger energy calibration is discussed is sect. 4.1.4).

In addition, a very-high threshold (typically 39 GeV) single-arm trigger with downscale factor of two was also used during most of the data taking period. It allows a cross-check of the efficiency of the Bhabha coincidence trigger. A very-low (typically 9 GeV) threshold single-arm trigger was also operating. It is used to estimate the beam-related background contamination to Bhabha scattering.

4 Cluster reconstruction

Showers are identified in each calorimeter by the reconstruction program (JULIA) using the energy deposited in each hit pad. A typical event display is shown in Figure 5. In the first pass of the reconstruction, the energies were obtained by applying the ADC conversion factor (5 MeV/ADC count). In a second pass the events were reprocessed using the full energy calibration discussed in the next subsection.

A simple and robust clustering algorithm was developed for the luminosity needs: it reliably locates electromagnetic showers without, however, separating a possible nearby cluster from a radiated photon. It supplies cluster quantities used for the energy and acoplanarity cuts, but its radial barycenter is only used indirectly in the radial fiducial cut (see the next section).

In each calorimeter a cluster starts from a pad with an energy above the "seed" energy ($E_{seed} = 300\ MeV$). As the shower maximum is typically reached between layer 3 and 4, the search is started more efficiently in layer 3, and then proceeds to deeper layers if no "seed" is found.

Additional neighboring pads are connected to the cluster if their energy is larger than the "single pad" minimum energy ($E_{min} = 30\ MeV$). This energy is 10 MeV above the ADC readout zero-suppresion threshold (ref. Sect.2). The pad's 8 adjacent neighbors in the same z-layer (k^{th} layer) can be *connected* by a common side or a corner in the (R,ϕ) plane; *connection* in depth is only possible in the $k-1$ or $k+1$ layers for the same radial bin. Two pads (same R but adjacent ϕ-bins) can be *connected* in these $\pm$ 1 layers to account for the 3.75° ϕ staggering in the calorimeter stack.

Known dead pads are accounted for during cluster formation as follows: cluster *connections* are allowed by skipping through a single dead pad to add a pad with energy $\geq E_{min}$.

Figure 6 shows the distribution of the total number of pads per cluster for the accepted Bhabha events; the mean number is 91.3 $\pm$ 10.1 pads averaged over the acceptance. The total number of pads per cluster for 40 to 50 GeV clusters, shown in Figure 7, falls smoothly with radius from 91 pads at the inner fiducial cut to 82 pads at the outer cut, due essentally to the increasing pad-size with radius. The cluster is cut outside the fiducial region by the edge of the detector.

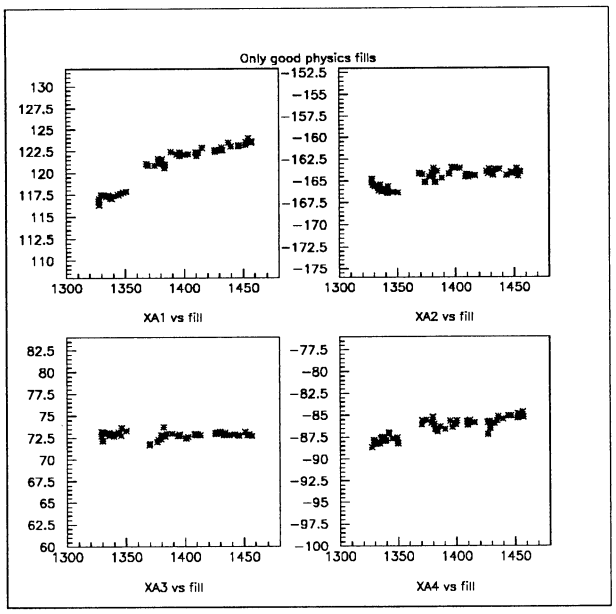

Figure 3: *Measurements (μm) of the relative x separations for module A versus fill number. Maximum drift is less than 8 μm. A3(front) and A2(rear) are at the top of the module, A1(front) and A4(rear) are at the bottom.*

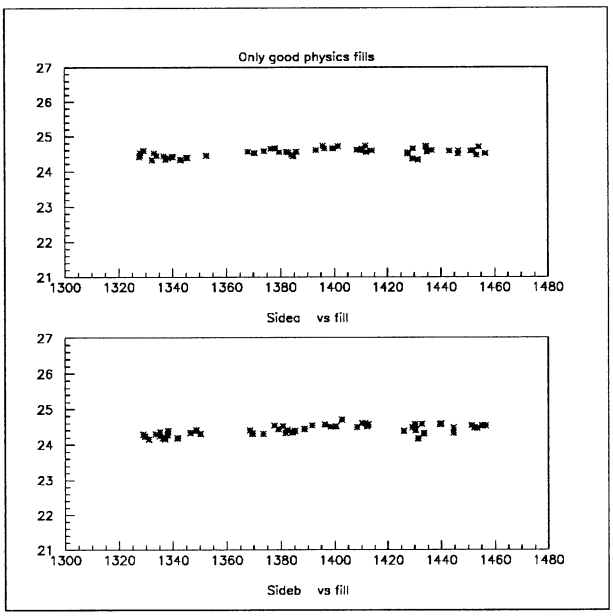

Figure 4: *Temperature measurements (deg. C.) for module A versus fill number. The r.m.s. variation is less than 0.3° C.*

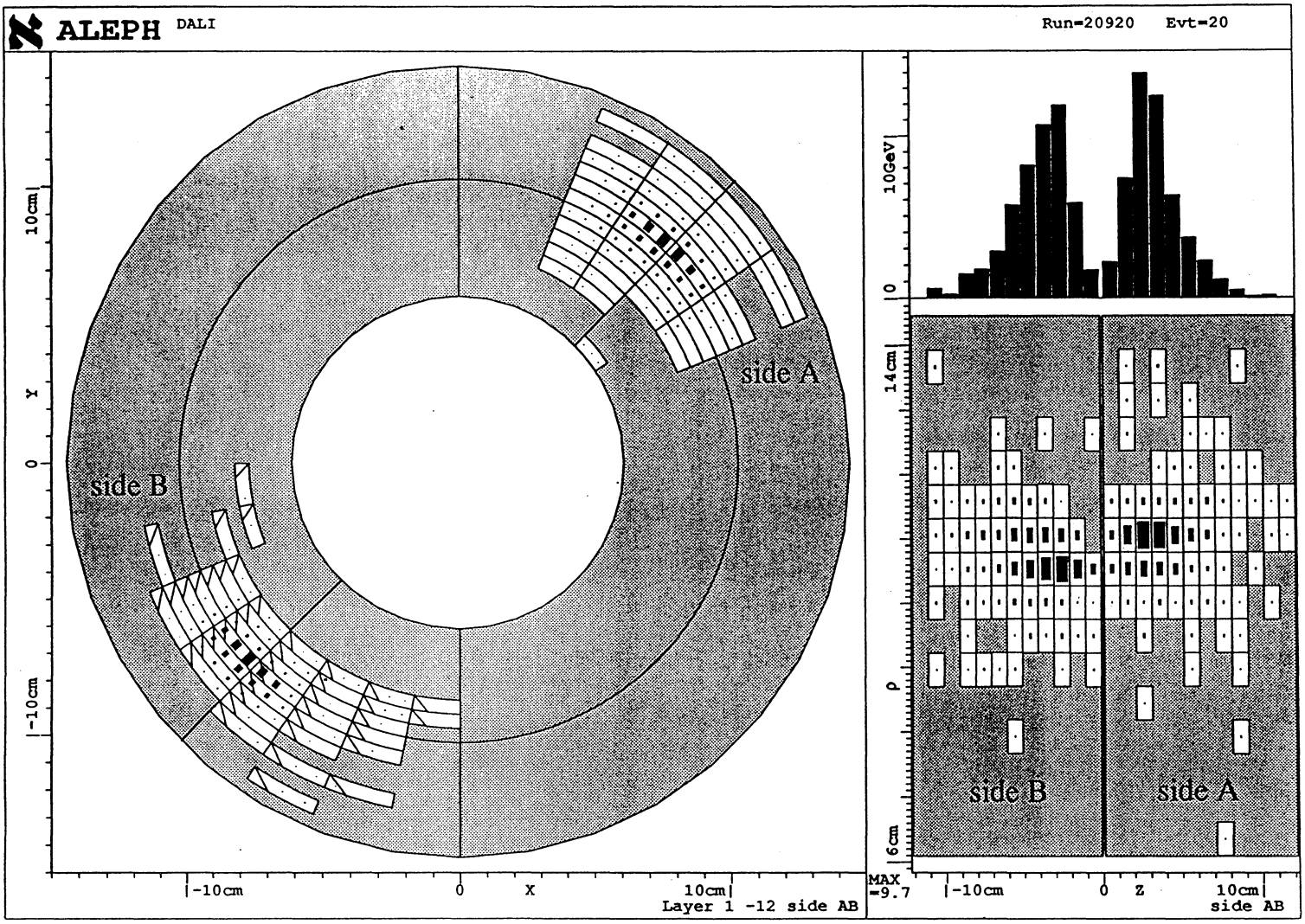

Figure 5: *Typical Bhabha event display (DALI). Clusters on A and B side are shown in same view. The Z-profile shown is the sum of energies over R-ϕ for each side; the center is the interaction point.*

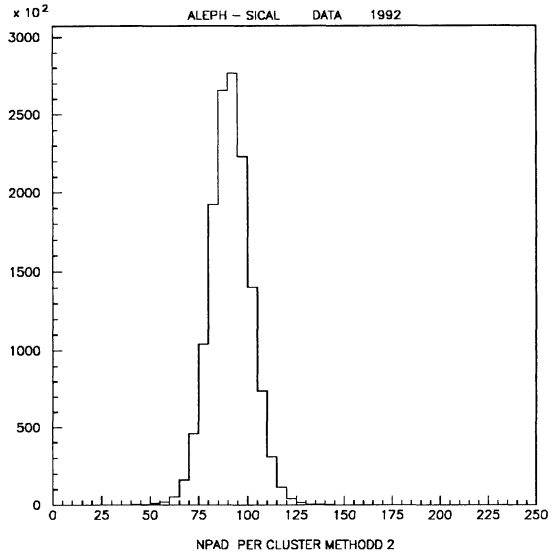

Figure 6: *Total number of pads per cluster for DATA (Bhabha event selection).*

The low value of E_{min} required to connect pads in a cluster ensures that an electron/positron shower and a possible radiated photon shower are merged into the same cluster within separations up to about 16 mrad.

As mentioned above, each cluster is characterized by its total energy and its barycenter position (R,ϕ and z). Radial and ϕ periodic corrections are applied to account for the "snake" effect due to barycenter method (ref. ALEPH Handbook, Chapt. IV sect. 6.1.3); an additional radial barycenter correction is included due to pad curvature and edge effects (see discussion of parametrization systematic errors). The barycenter correction added to the radial position is given by the formula:

$$Corr_R^{bary} = a_1 \sin(2\pi R_{clus} + a_2 \sin(2\pi R_{clus})) \tag{3}$$

where $a_1 = -0.030\ cm$ and $a_2 = 0.325$.The formula for the ϕ correction which is added to the ϕ position is complicated by the off-set of each successive layer in ϕ:

$$Corr_\phi^{bary} = \sum_{i=1}^{3} b_i \sin(2\pi\phi_i^{clus} + c_0 \sin(2\pi\phi_i^{clus})) \tag{4}$$

where ϕ_i^{clus} is the cluster ϕ-barycenter shifted by the layer's corresponding ϕ-offset, b_i = -0.0438, -0.0450 and -0.0449, and $c_0 = 0.500$.

4.1 Energy response

4.1.1 Pedestal measurement and stability

Pedestals were recorded at every global Aleph calibration procedure which occurs essentially at the beginning of every LEP fill. Since pedestals and gains are affected by the input capacitance of the front-end amplifiers, pedestals are recorded with High Voltage ON. Typically the σ of the pedestal means is $\approx$ 3.5 MeV (0.7 ADC counts, where 1 ADC count $\simeq$ 5 Mev).

The stability of the pedestals has been monitored during all the 1992 data taking. The mean pedestal drift was $\leq$ 20 MeV during this entire period, with the largest shift due to the transition from 4 bunch to 8 bunch mode for LEP. The fill to fill drift of the means was always $<$ 2 MeV. The main source of pedestal shift is attributed to low voltage variations which induce coherent shifts of about 0.3 MeV/mV for changes of either the +5 V or -5 V power supplies.

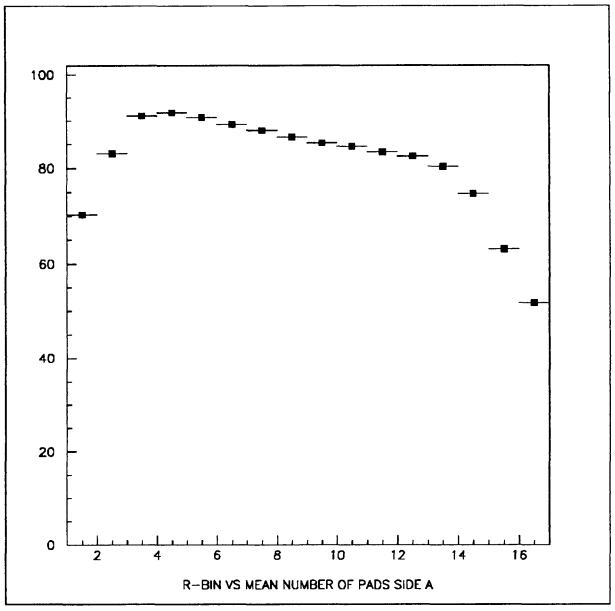

Figure 7: *Number of pads per cluster for DATA plotted versus R_{clus}-bin; coplanar clusters ($\Delta\phi$ cut) selected for energies between 40 and 50 GeV. Bhabha selection fiducial region: pads 4 to 12 inclusive.*

4.1.2 Energy calibration: (1) Electronic gain calibration

Pad to pad energy calibration is obtained by measuring the response of each amplifier channel; this is achieved by pulsing individual channels (simultaneously on all the amplifiers). Both gain and inter-channel crosstalk are measured. Five injection levels are used to determine the amplifier response curve, which is fitted to a parabola. The amount of calibration constants is reduced from 36864 to 3856, by fitting to an average gain per chip. This was justified on the basis of series measurements of the AMPLEX gain behaviour from channel 1 to 16. The residuals of this fitting procedure are below 0.7 %. In addition, subsequent checks were made for bad channels (disconnected pads, broken capacitors and faulty AMPLEXes)

4.1.3 Energy calibration: (2) Off-line corrections

Applying the gains obtained from the electronic calibration improves the resolution for fully contained 45 GeV showers from 6.2% to 5.5%. Nevertheless additional corrections discussed here are needed to obtain a uniform energy response over the detector in radius and ϕ.

First, dead pads or AMPLEXes were identified from the longitudinal profile for showers centered in each of the 16 radial and 32 azimuthal pads in each of the two SiCAL modules. Altogether one dead AMPLEX (16 pads) and 14 individual dead pads were identified. On the same basis, two crystals with low gain, for which the electronic calibration did not adequately compensate, were identified. The linear component of the gains for the affected channels was increased by a factor of two in order to correct the longitudinal profile.

Second, it was necessary to correct the global radial gain dependence from the electronic gain calibration. Three different sources can contribute to radial gain variations which can not be measured by the electronic calibration: (1) AMPLEX hold timing differences between data taking and calibration runs ($\simeq$ 20% shift over 16 channels for 300 ns delay), (2) Radially dependent gain non-linearities, and (3) Cross-talk between neighboring pad rows on the same crystal. Although these effects are small, they can directly influence the luminosity selection for the fiducial cut pad rows (see discussion sect. 5.3). The size of the effect (and corrections) for these pad rows is shown in Table 3. The systematic error arising from this correction is discussed in section 7.5.1. The resulting mean cluster energy for Bhabha events as a function of radial pad row is shown in Figure 8. Shower leakage near the detector edges is responsable for the energy loss in those regions.

Third, several global ϕ corrections were made to account for other effects not accounted for in the electronic calibration. The first of these is a physical effect due to the layout of the silicon wafers in each layer of the detector. Neighboring crystals are staggered in the z direction, in order to allow them to overlap in ϕ, so that the gap traversed between the preceeding (following) layer of tungsten and the silicon alternates. There are two consequent

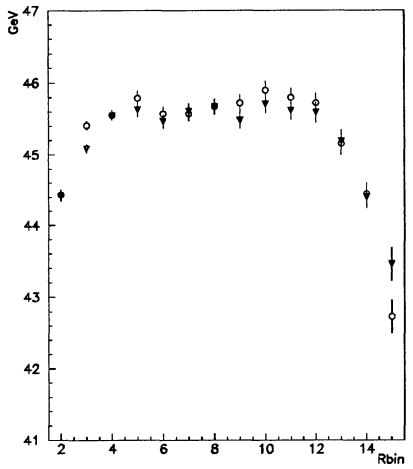

Figure 8: *Mean cluster energy of Bhabhas versus radial bin after final corrections. A-side shown as full triangles and B-side as open circles.*

physical effects which have been identified [9]. One involves the absorption of soft electrons in the air gap reducing the signal in the silicon as the space increases, and the other the backscattering of the shower constituents from the following tungsten plate. This effect is corrected by increasing the gain applied to alternate crystals by 4%. The size of the correction was obtained empirically.

The other two ϕ corrections are related to the organization of the electronics components. A gain correction of 3% was made for alternate azimuthal bins which correspond to the two AMPLEX chips on one "daughter" board. A variation in gain across each half-module, corresponding to each "mother" board (low voltage distribution), was also observed. For side A this correction was

$$0.07 \left| \frac{(\phi - \pi)}{\pi} \right|, \; 0 < \phi < 180°, \tag{5}$$

$$0.07 \left| \frac{(\phi - 2\pi)}{\pi} \right|, \; 180 < \phi < 360°, \tag{6}$$

and for side B,

$$0.09 \left| \frac{(\phi - N\pi)}{\pi} \right|, \tag{7}$$

where N is the number of the detector half.

Despite all of these corrections, some residual variation from one ϕ sector to another remains, and a final *ad hoc* correction factor was applied for each of the 32 azimuthal bins in each module (A,B). The root mean square

	Gain Difference			
	Pad rows 2-1 (Inner loose cut)	Pad rows 4 - 3 (Inner fiducial cut)	Pad rows 13 - 12 (Outer fiducial cut)	Pad rows 16-15 (Outer loose cut)
(1) Electronic calibration	1.2%	0.18%	0.75%	-3.24%
(2) Final Correction used	1.2%	0.18%	0.00%	0.00%

Table 3: *Global radial gain correction for fiducial cut pad rows. (The difference between the electronic calibration and the final correction is included in the overall systematic error).*

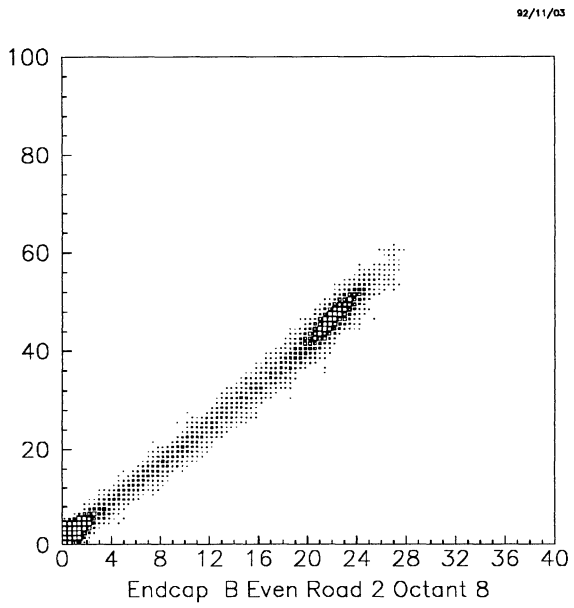

Figure 9: *Trigger signal versus read-out energy for a typical trigger sector. Sectors contain only odd or even planes, so the Bhabha events form a peak at half the beam energy.*

deviation of these factors from 1 is 1.6% and the mean deviation is 1.2%. These ϕ corrections do not enter into the radial fiducial cut for the luminosity selection discussed later.

The final energy resolution after corrections is 4.9%.

4.1.4 Energy calibration: trigger

The energy response of the trigger is established using the digitized output from all 64 trigger sectors. This signal is compared with the calibrated energy measured in the MUX ADC's. Figure 9 shows a plot of trigger energy versus Mux ADC energy. A linear fit is made to this plot for each trigger sector every fill. The overall r.m.s. variation (sector-to-sector and fill-to-fill) of the slope was 4%, and the variation of the trigger pedestals was 2 GeV.

5 Event selection

The Bhabha events are selected from SiCAL coincidence triggered events on the basis of the following "luminosity" selection:

- Two reconstructed clusters are required (at least one on each side).
- Energy of largest cluster on each side $\geq$ 20 GeV and their sum $\geq$ 55 GeV.
- Radial fiducial cuts (one cluster within a "tight-acceptance", and the opposite within a "loose-acceptance").
- Acoplanarity cut based upon two largest cluster's ϕ-difference.

The fraction of events rejected by the different cuts is summarized in Table 4. Additional selections, either relaxed radial cuts or special ϕ selections (discussed in sect. 5.3 and 7.8), are used for luminosity selection cross-checks.

5.1 Reconstructed cluster cut

The signature of a typical Bhabha event is two "back to back" electromagnetic clusters. The requirement of at least one reconstructed cluster in each endcap (Side A and Side B) ensures this condition. Since Bhabha events generally have radiated photons which may or may not be distinguishable from the "primary" cluster, no upper limit on the number of clusters found is imposed. Table 5 shows number of reconstructed clusters on Side A versus Side B per event (SiCAL coincidence trigger), before luminosity selection. Most of the events (97.5 %) have $\leq$ 3

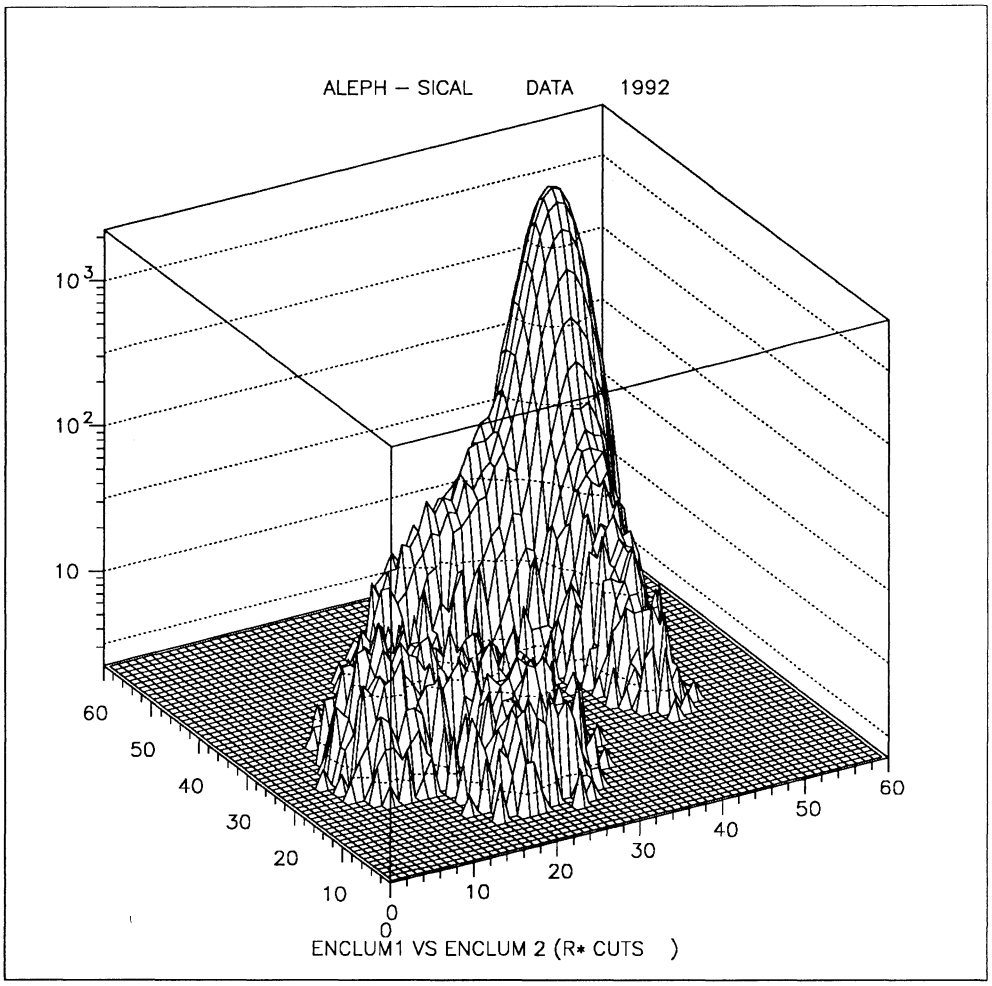

Figure 10: *Largest reconstructed cluster energy on Side-A versus largest reconstructed cluster energy on Side-B (GeV).*

reconstructed clusters. The low noise level of the trigger is apparent in the absence of single-arm reconstructed clusters in the coincidence triggered event sample.

5.2 Energy cuts

In order to ensure trigger efficiency, the cluster energy in each SiCAL module $E_{A,B}$ is required to be greater than or equal to 20 GeV. Furthermore, to separate the Bhabha signal from background due to random coincidence of off-momentum beam particles, a cut is made on the sum of the two energies, $E_A + E_B \geq 55$ GeV. The reconstructed energy for the largest cluster in module A is plotted versus the largest cluster energy in module B in Figure 10. The largest cluster energy distribution after cuts is shown in Figure 11. Events in the high energy tail of the distribution were scanned and are consistent with accidental coincidences of Bhabha events with off-momentum beam background.

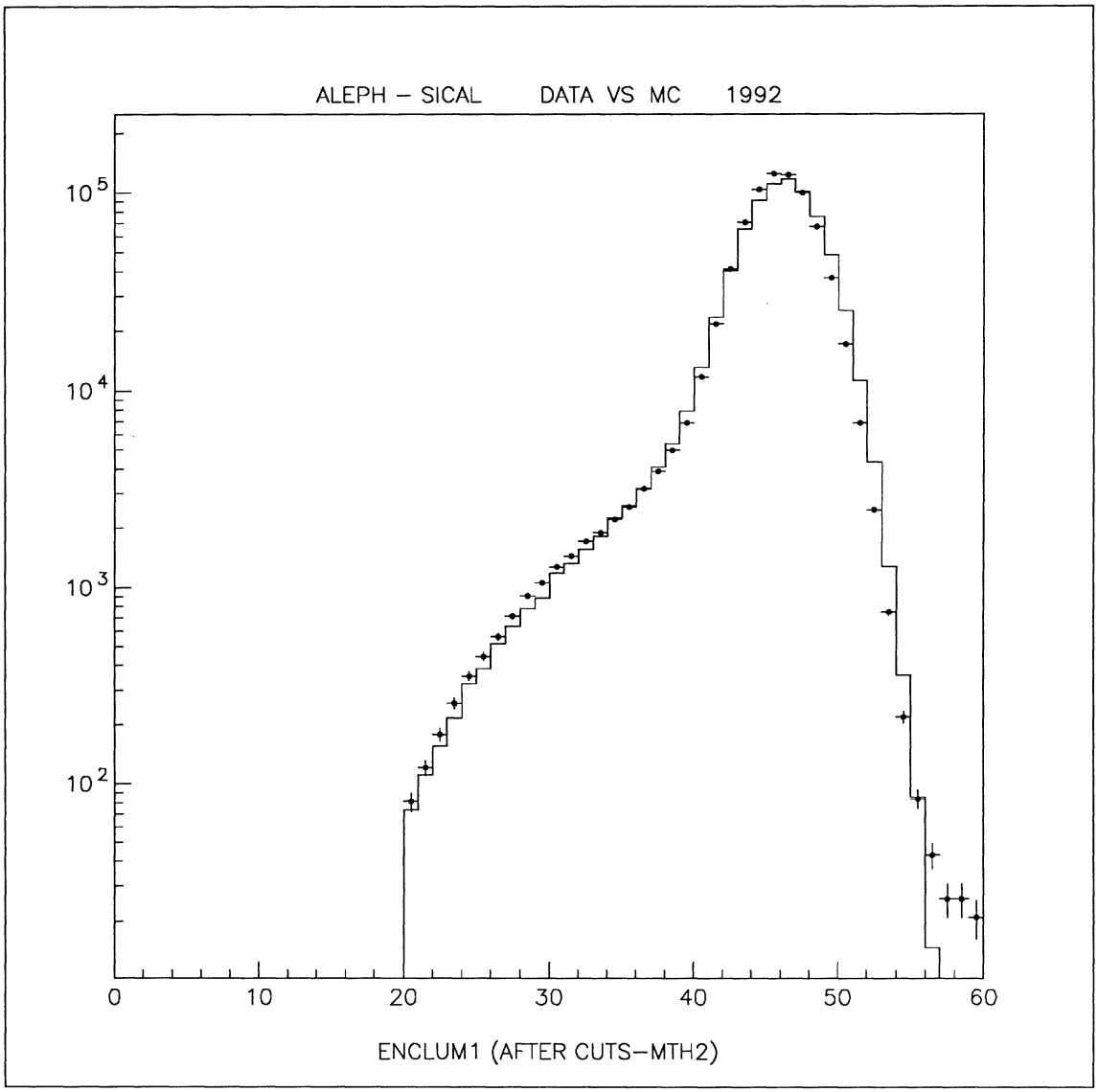

Figure 11: *Largest cluster energy distribution (Side-A) after Bhabha event selection (GeV). Data are plotted as points; Monte Carlo is shown as a line.*

(1) ≥ 1 reconstructed cluster on each side	nil
(2) Energy cuts	14%
(3) Radial fiducial cuts	43%
(4) Acoplanarity cut	$\leq 1\%$
TOTAL fraction rejected	58%

Table 4: *Fraction of SiCAL coincidence-triggered events rejected by luminosity cuts (fractions depend upon order of cuts).*

	Number of clusters (Side A)					
	0	1	2	3	4	5
0	0.00%	–	–	–	–	–
1	–	83.14%	6.73%	0.56%	0.06%	0.01%
2	–	7.66%	0.72%	0.08%	0.01%	–
3	–	0.80%	0.07%	0.01%	–	–
4	–	0.11%	0.01%	–	–	–
5	–	0.02%	–	–	–	–

Table 5: *Number of reconstructed clusters per event on Side A versus Side B before luminosity selection.*

5.3 Radial fiducial cuts

The role of the radial fiducial selection is to precisely define the acceptance of the measured cross-section, in contrast to the other selection criteria which are used to separate "Bhabha" event candidates from possible backgrounds. Furthermore, the steeply falling t-channel cross-section places more importance on the inner radial fiducial cut; at small angles the lowest order Bhabha cross-section is simply:

$$\frac{d\sigma}{d\Omega} = \frac{16\,(\hbar c\alpha)^2}{s}\left(\frac{1}{\theta^4}\right) \tag{8}$$

which gives:

$$\sigma_{measured} = \frac{1040\ nb\ GeV^2}{s}\left(\frac{1}{\theta^2_{min}} - \frac{1}{\theta^2_{max}}\right) \tag{9}$$

where the angular bounds can be defined as radial limits at a defined z-distance from the interaction point: $\theta_{min} \rightarrow R_{min}$ and $\theta_{max} \rightarrow R_{max}$.

In order to reduce the sensitivity of the measurement to possible z-displacements of the beam (or z-offsets of the beam-SiCAL system, see section 7.4) and to loosen the colinearity constraint on radiative Bhabha events at the fiducial boundary, two fiducial cuts are employed: a "tight-side" restricted selection and a "loose-side" less-restrictive cut. The "tight" and "loose" sides are alternated each event (see sect. 7.4). The basic luminosity selection requires the "tight-side" cluster to lie within radial pads 4 to 12 (inclusive), while the "loose-side" cluster in the other calorimeter is accepted if it is within radial pads 2 to 15 (inclusive). Selecting on the "tight-side" at the inner radial edge of the 4th pad assures the independence of the fiducial cut with respect to both the total energy (reference Figure 8) and the cluster size (ref. Figure 7). Additional selections are used to cross-check the final results and are discussed in Sect. 7.8.

In order to determine whether a cluster is inside the fiducial region, we define

$$A_r = \frac{E_{in} - E_{out}}{E_{in} + E_{out}} \tag{10}$$

("radial energy asymmetry") where E_{in} is the energy inside a radial padwidth within the fiducial region and E_{out} is the energy in the radial padwidth outside. Figure 12 shows the variation of the radial energy asymmetry as a function of the cluster radial position near the inner fiducial boundary.

Single radial strips are used to make up the partial energy sums, E_{in} and E_{out}, used for this selection. This minimizes possible effects from leakage near the edge of the detector, and reduces sensitivity to the Monte Carlo simulation of the electromagnetic shower transverse distribution. The strips are summed over two adjacent ϕ-bins: one including the ϕ of the full cluster barycenter and the other, that neighbor making up the largest partial energy sum. The double ϕ-bin wide strips are summed in depth to reduce the size of the energy fluctuations, however this is limited to two layers in depth in order to minimize the effect of the "non-projective" geometry of the SiCAL pads (ref. section 2): layers 3 (6 Xo) and 4 (8 Xo) are summed for the "tight" selection; layers 3 (6 Xo) and 5 (10 Xo) are summed for the 1992 "loose" selection. Several dead pads (detectors subsequently replaced in 1993) in the outer radii of layer 4 motivated the choice of layer 5 for the "loose" selection. The double ϕ-bin strip width is required because of the 3.75° staggering in ϕ between successive layers. Figure 13 shows the E_{in} versus E_{out} distribution of the partial energy sums used to define A_r near the inner fiducial boundary.

The radial distribution of events (passing the energy and $\Delta\phi$ selections) is shown for the "tight-side" selection (including an additional inner radial pad) in Figure 14 and for the "loose-side" selection (including additional pads both above and below the loose-side radial cuts) in Figure 15. The comparison with the Monte Carlo simulation is shown in both figures; the agreement is excellent.

5.4 Acoplanarity cut

Bhabha events are essentially coplanar, except for radiated photons. A selection on the ϕ-difference between "tight-side" and "loose-side" largest cluster barycenters, $\Delta\phi$, was optimized to keep as much of the "radiative tail" as possible, while removing accidental coincidences of off-momentum beam background. Events are accepted for the range:

$$150° \leq \Delta\phi \leq 210°. \tag{11}$$

The $\Delta\phi$ distribution for data and Monte Carlo (no background) are shown in Figure 16. The sources of excess events seen in the data outside the Bhabha peak are discussed in the next section.

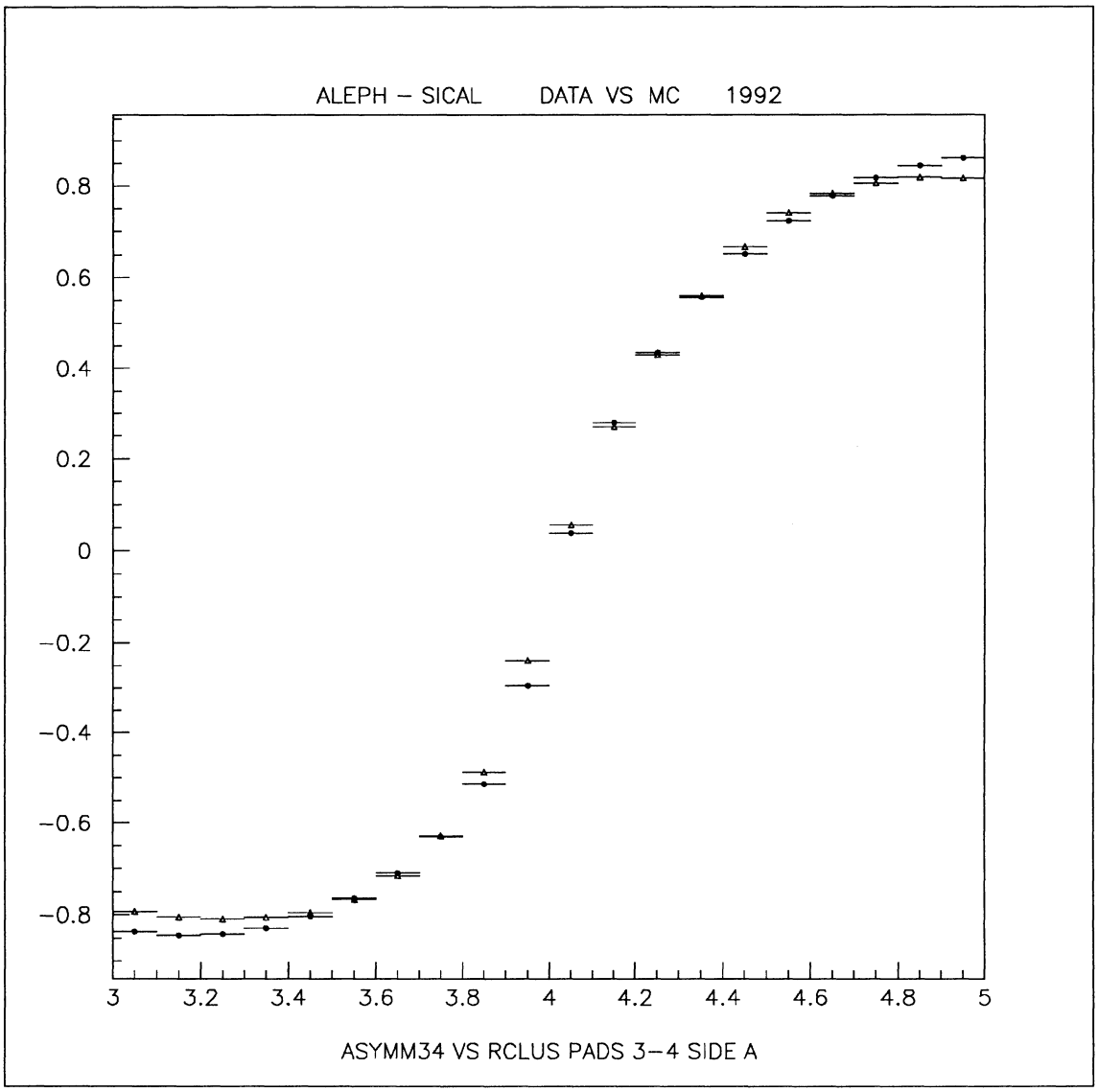

Figure 12: *The radial energy asymmetry, A_r shown versus the cluster radial position near the pad 3-4 boundary. Data are shown as full squares and Monte Carlo as open triangles.*

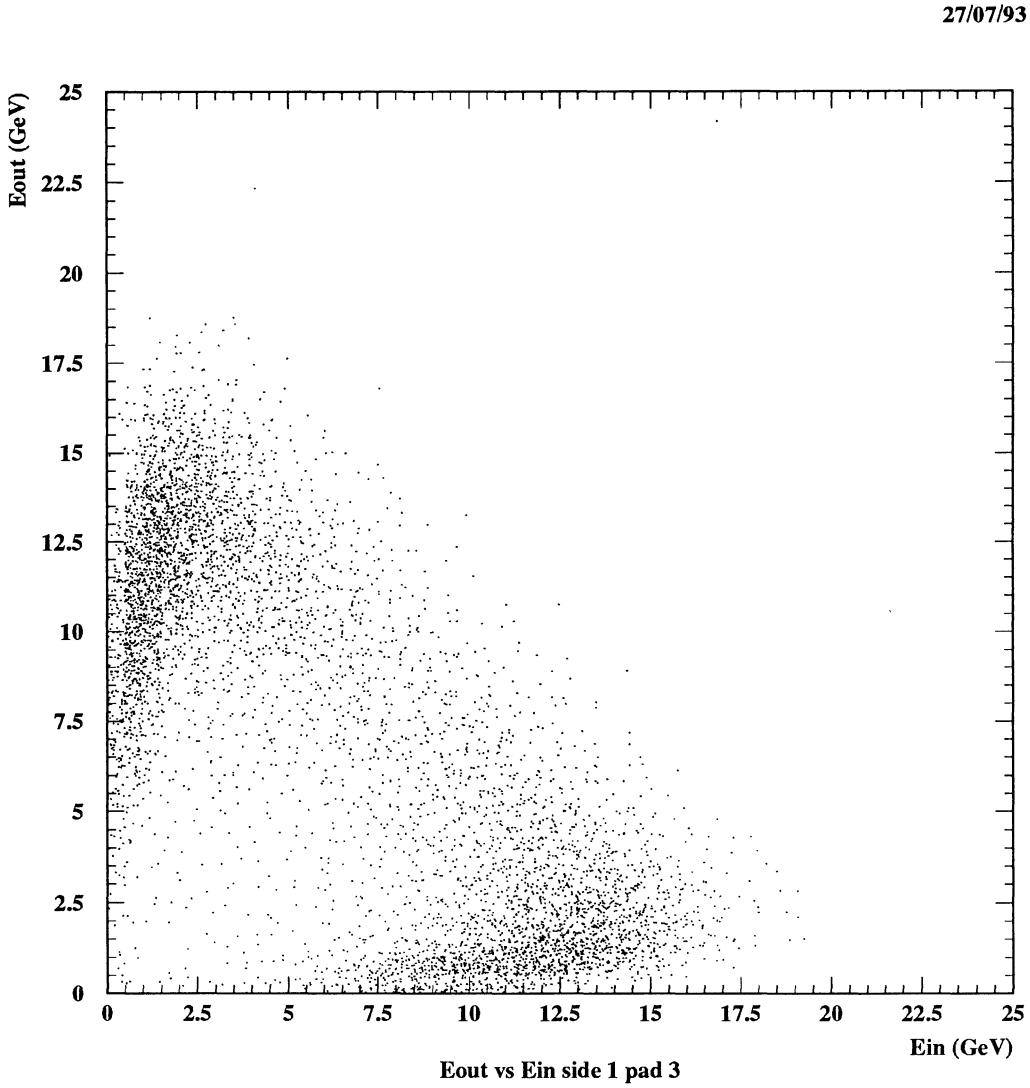

Figure 13: *E_{in} versus E_{out} for events passing the energy selection and having a cluster barycenter in the pad 3 to 4 region. Bands near the axis are showers centered on the respective pads.*

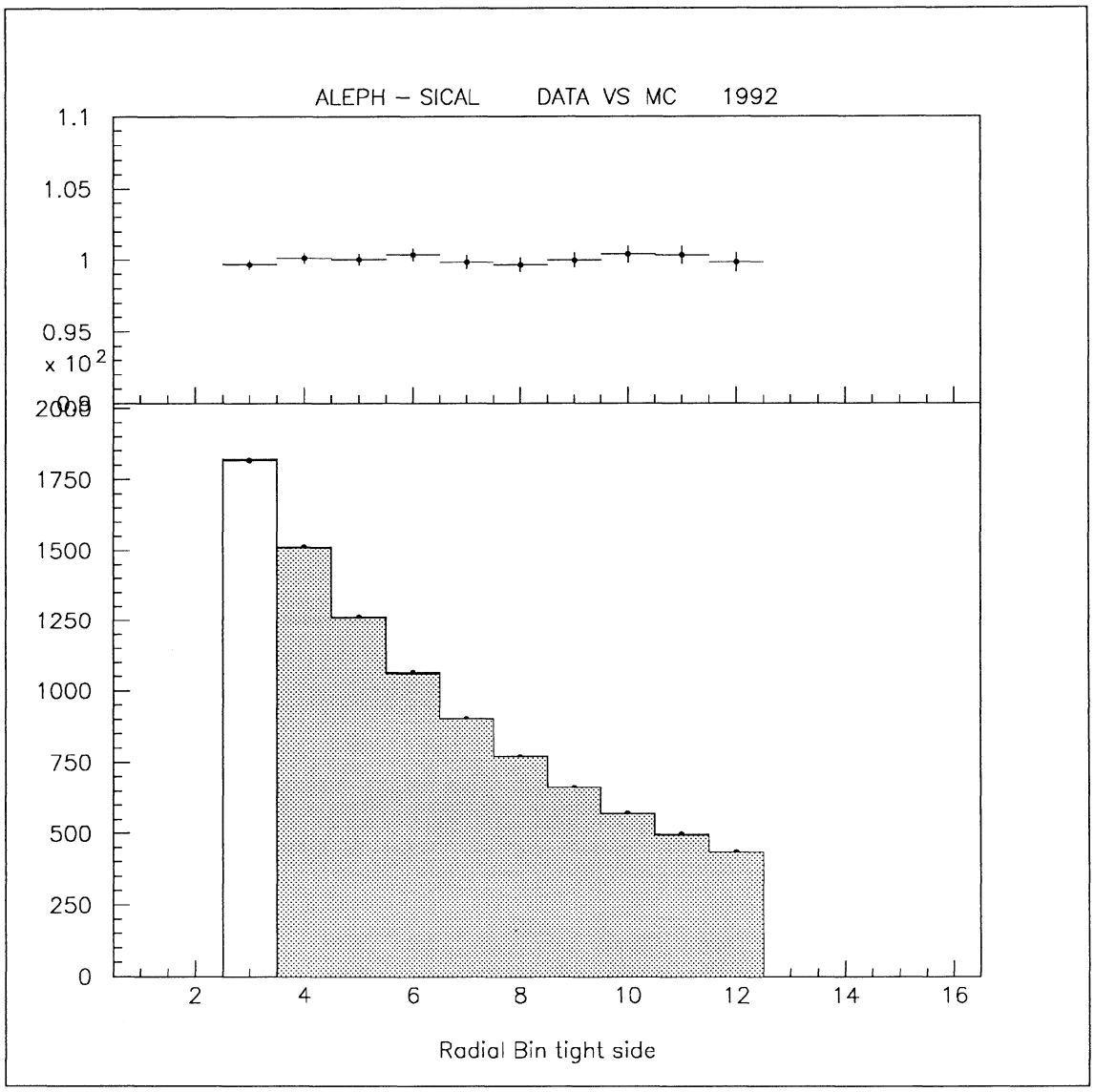

Figure 14: *Radial distribution for "tight-side" selection (final selection shown as hashed zone), insert shows ratio of DATA to Monte Carlo. Data are plotted as points; Monte Carlo shown as a line.*

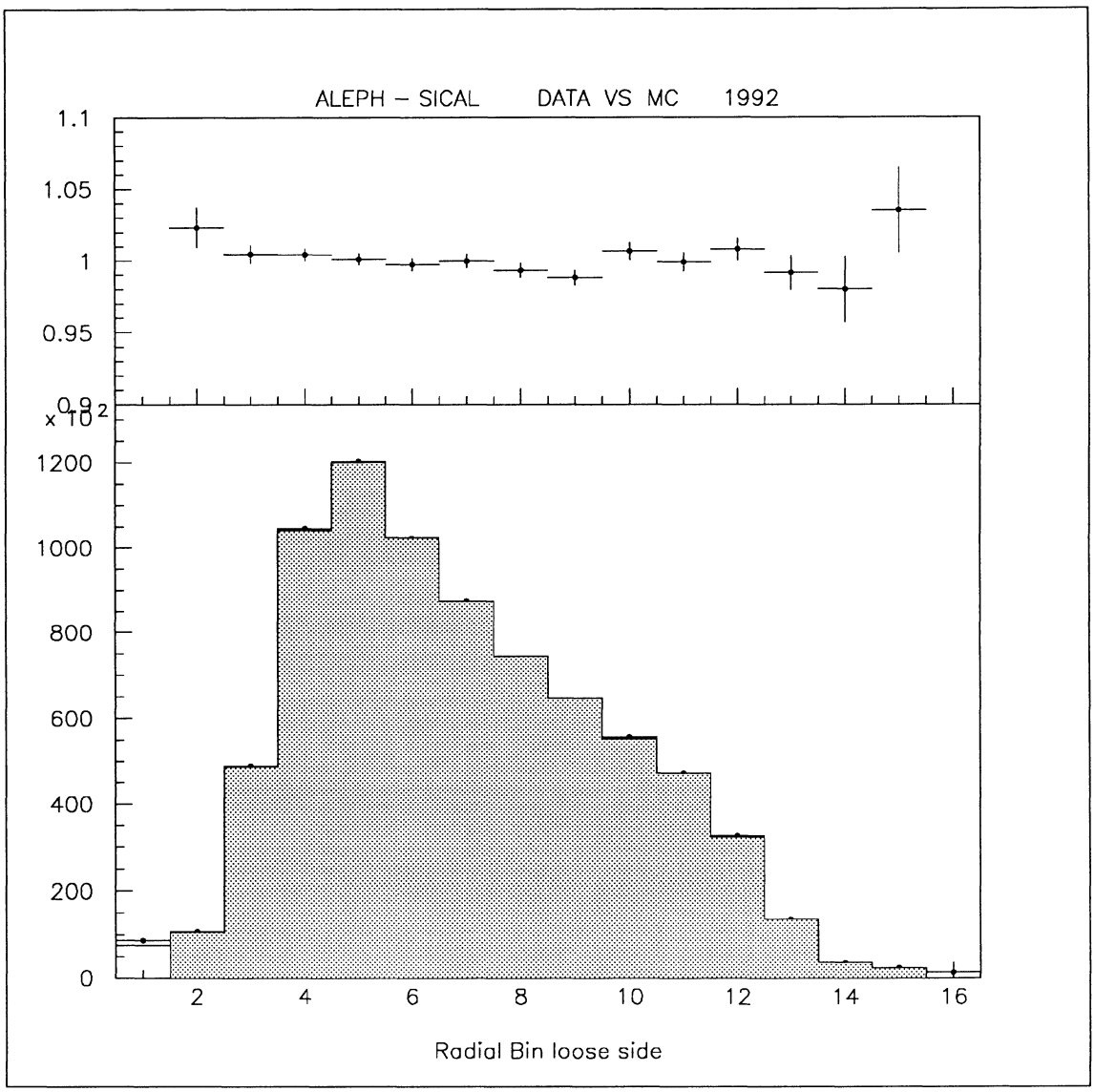

Figure 15: *Radial distribution for "loose-side" selection (final selection shown as hashed zone), insert shows ratio of DATA to Monte Carlo. Data are plotted as points; Monte Carlo shown as a line.*

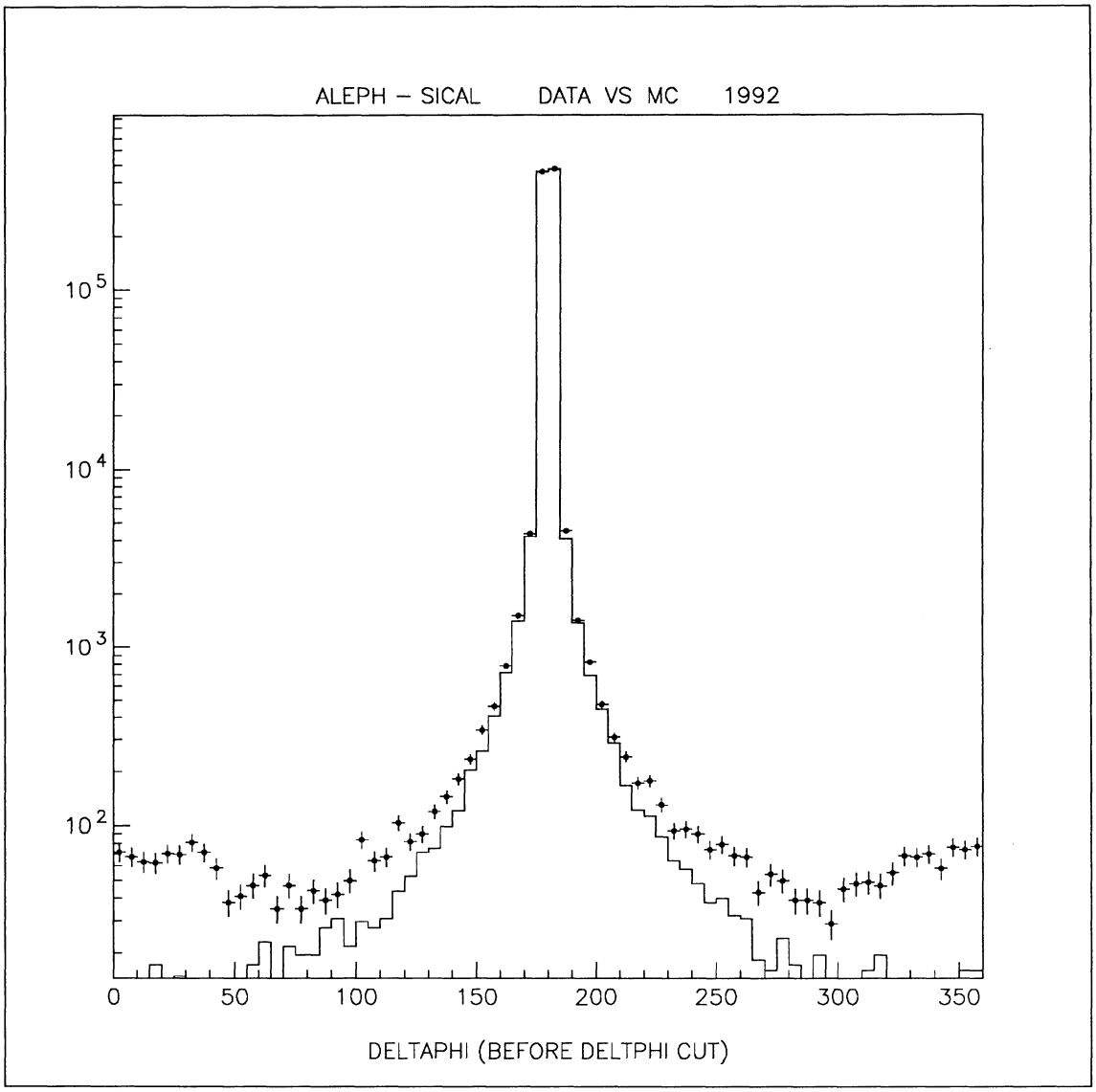

Figure 16: *Distribution of the ϕ-difference $\Delta\phi$ between the "tight-side" and "loose-side" clusters. Data are plotted as points and the Monte Carlo is shown as a line.*

6 Background

Backgrounds to the Bhabha cross-section measurement can come from two areas: (1) machine related particles which "fake" coincidence triggers or which disturb otherwise valid Bhabha events, and (2) "physics" processes which give events with electromagnetic clusters which pass the luminosity selection. Fortunately, the LEP environment is clean enough to limit the first category primarily to off-momentum beam particles. The treatment of the data sample has been done differently for both areas: the beam related backgrounds, which are fill dependent, are subtracted from the data, whereas the physics background has been treated as a cross-section correction (see section 9). The estimation of both of these background sources and the respective uncertainties are discused in the two following sub-sections.

6.1 Off-momentum beam particles

A background to Bhabha scattering comes from off-momentum particles in the LEP beam which spill out and strike the SiCAL calorimeters. When this coincidentally happens in both calorimeters at the same time, the event may satisfy the coincidence trigger and occasionally pass the luminosity cuts. A single-arm trigger with a very low threshold of 9 GeV (typically) is used to estimate the rate at which this happens by measuring the rate and distribution of beam-related background in both calorimeters.

The calculation is performed in two steps. First, the rate at which off-beam momentum electrons and positrons satisfy the coincidence trigger is calculated for those particles passing the 20 GeV cut on both sides. Then the fraction of those accidental-coincidence events passing the remaining cuts is determined.

The error in the calculation is estimated by comparing the calculated background to the observed background in a region which is (largely) devoid of signal. The extent to which the prediction and the measurement disagree is taken as the systematic error in the background calculation.

6.1.1 Rate of triggering background with E_a, $E_b \geq 20$ GeV

Events within our acceptance are required to have $E_a \geq 20$ GeV and $E_b \geq 20$ GeV, and to trigger they must have satisfied the trigger conditions $(A_{high} \bullet B_{low} + A_{low} \bullet B_{high})$. In a background event, either side may have fired the high threshold, the low threshold, or neither threshold. The two-sided event therefore has nine possible trigger masks, shown in Table 6, of which only three trigger the readout. The rate of triggering events can be constructed by calculating separately the rate of the three boxes which trigger the coincidence readout and then add them up. This gives:

$$f_{Acc} = (f_H^A f_H^B + f_H^A f_L^B + f_L^A f_H^B)/\nu \tag{12}$$

where f_{Acc} is the rate of accidental coincidence triggers, f_H^A and f_L^A are the rates of the high and low (only) trigger on the A-side, f_H^B and f_L^B are the same on the B-side, and ν is the beam crossing frequency (45 kHz with four bunches in the machine and 90 kHz with 8 bunches in the machine).

However what is needed is the rate of triggering events in which the most energetic cluster on each side is above 20 GeV. Instead of using raw trigger rates in the right-hand-side of equation 12, the rates for the most energetic showers above 20 GeV are used:

$$f_{Acc}^{20} = (f_{20,H}^A f_{20,H}^B + f_{20,H}^A f_{20,L}^B + f_{20,L}^A f_{20,H}^B)/\nu \tag{13}$$

These rates are measured by counting the number of clusters, on either side, fullfilling the given trigger conditions and with energies above 20 GeV, and then dividing by the "live time", which is related to the number of random triggers.

TRIGGER MASK	A : neither	A : Low only	A : Low and High
B : neither	No	No	No
B : Low only	No	No	Yes
B : Low and High	No	Yes	Yes

Table 6: *Trigger masks: A-side versus B-side. Only three masks trigger the coincidence readout. "Low" and "High" refer to the 12 GeV and 24 GeV thresholds respectively.*

A correction factor is applied arising from the possible correlation of background levels on both sides. One known source for such a correlation, is the slow loss of beam current during a fill. The equation above consists of terms like $f^A \bullet f^B$, where the measured rates calculated as above are averaged over the fill, i.e. $< f^A > \bullet < f^B >$, which are products of averages. Since averages of the products is really what is required, i.e. $< f^A f^B >$, the calculated rate is corrected by the factor (evaluated from the single arm low threshold trigger rates):

$$\frac{< f^A f^B >}{< f^A >< f^B >} = \frac{< f^A f^B > + < f^A >< f^B > - < f^A >< f^B >}{< f^A >< f^B >} \tag{14}$$

$$\frac{< f^A f^B >}{< f^A >< f^B >} = 1 + \frac{Cov(f^A, f^B)}{< f^A >< f^B >} \tag{15}$$

which is nonzero when changes in the background levels on both sides are correlated. The correction averaged with respect to the fill luminosities over the 1992 SiCAL running period is +11%.

6.1.2 Fraction of events passing additional cuts

A simplified version of the luminosity analysis is used to estimate the background contamination. In this case the asymmetry radial fiducial cut is replaced by a cut on the barycenter radial position.

The data are analysed for each LEP fill. Single-arm event clusters with energies above 20 GeV are stored in separate arrays for A and B sides. Then all possible combinations of the two clusters are formed. Combinations satisfying the coincidence trigger are added to a subsample of artificially constructed background events. The method used to determine the expected rate for these events was shown in the previous section.

Next, all additional luminosity cuts are applied to the subsample:

- The radial fiducial cut
- The $E_a + E_b \geq 55$ GeV Cut
- The $\Delta\phi$ cut

In addition, the simplified luminosity analysis is applied to all coincidence triggers. Figure 17 shows the effect of the cuts on the coincidence triggers, and on the artificially constructed background.

The rate of triggering background events with E_a, $E_b \geq 20$ GeV, discussed in the last section, is reduced by the efficiency through the remaining cuts and compared to the Bhabha rate from the simplified luminosity analysis. The background rate is found to be lower than the Bhabha rate by a factor of 7.0×10^{-4}.

6.1.3 Beam-related background uncertainty

Coincidence triggers with E_a, $E_b \geq 20$ GeV, passing the fiducial cut but failing the cut $E_a + E_b \geq 55$ GeV (i.e. those below the diagonal cut in figure 17) are mostly background, with a small contamination of double-radiative Bhabha scattering events. The artificial events which lie in the same region may be compared with the observed events. In figure 18 (top) we compare the ϕ distribution (shape and normalization) of the predicted and the observed events. The bins at $\phi = 180°$ have a large contamination from double radiative Bhabhas. If we exclude the three central bins, the prediction is 20% lower than the measured rate. After increasing the prediction by this factor (figure 18 bottom) one can see that shape of the prediction agrees well with the observed shape. We also increase the prediction for the background contamination within the signal region by 20%, to 8.5×10^{-4} , and take 20% of this (1.7×10^{-4}) as the systematic error on background.

A second potential source of beam-related background effects on the luminosity measurement is the loss of valid Bhabha events due to a superimposed off-momentum beam particle. The valid event could be rejected by the $\Delta\phi$ cut if the background cluster had an energy superior to the Bhabha event's cluster on that side. The effect concerns good events in the radiative tails where the cluster energy measured in SiCAL is low. We have evaluated the effect using the fraction of Bhabha events below 35 GeV, compared with the single arm rate above 20 GeV. This gives an upper limit for the loss of good events of 5×10^{-5}.

6.2 Physics background contribution

Four different sources of physics background sources have been considered; their contamination to the selected Bhabha sample has been estimated either with the help of MC generators or by direct analytical calculations.

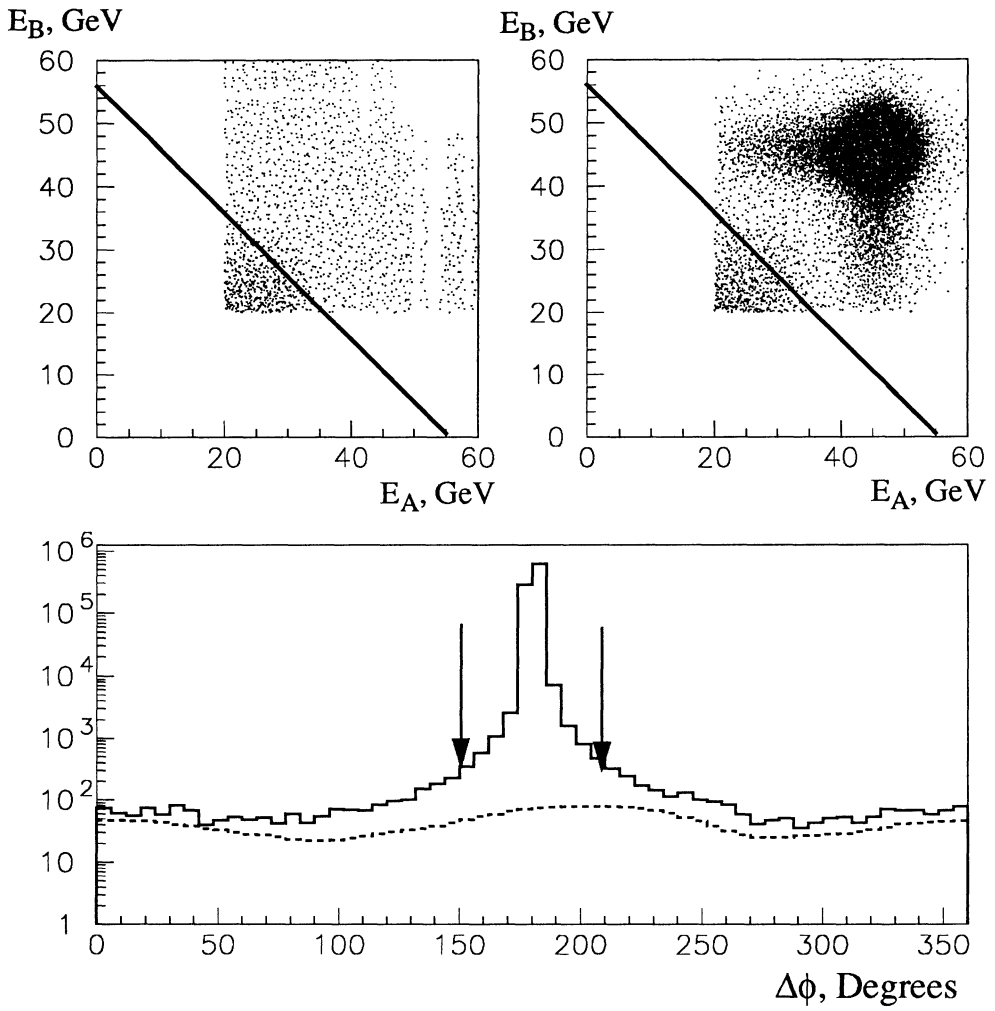

Figure 17: *Comparison of calculated background and observed signal+background. Top: Calculated background(left) and measured signal + background (right). The line indicates the cut* $E_a + E_b \geq 55$ *GeV. Bottom:* $\Delta\phi$ *distribution for events passing this cut. Dashed line is calculated background and solid line is measured signal + background. The arrows indicate the cut at* $150° < \Delta\phi < 210°$.

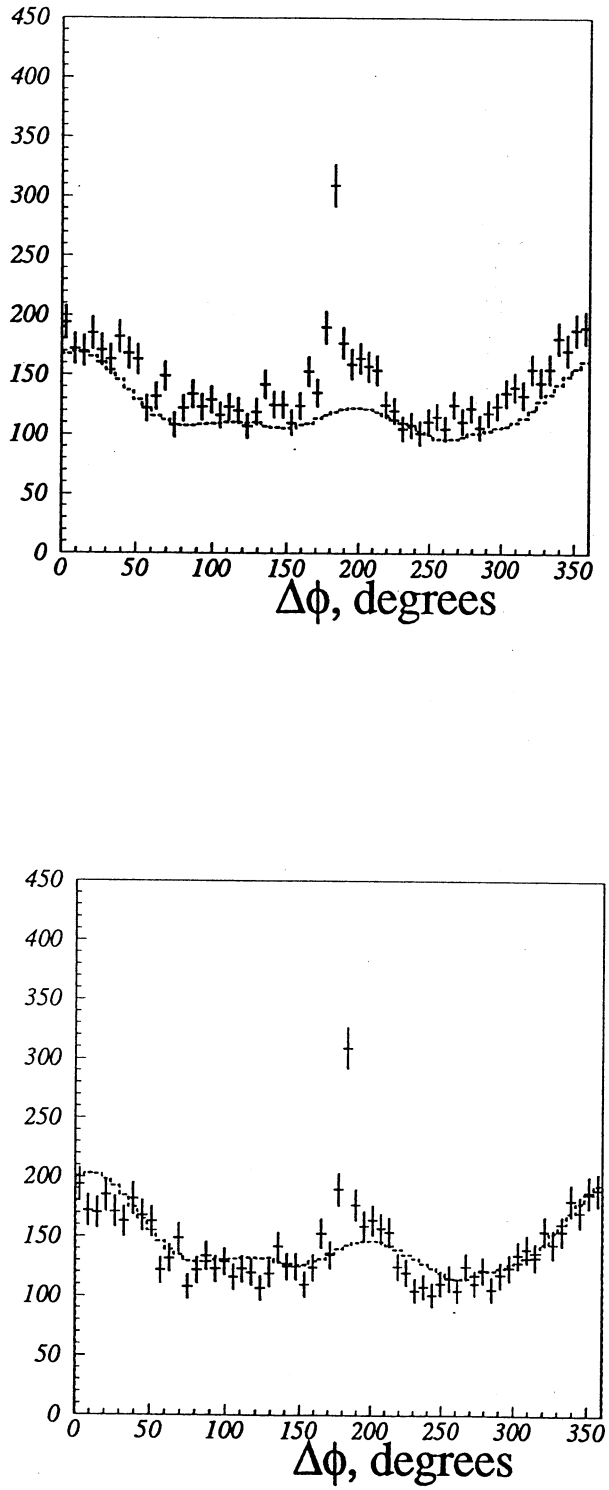

Figure 18: *Top: $\Delta\phi$ distribution of "background" events below the cut $E_a + E_b > 55$ GeV. Bottom: Same data (shown as points) however, here the calculated background (shown as a dashed line) has been adjusted upwards by + 20 % to better fit the observations. The peak at* 180° *is expected from doubly radiative Bhabha events with missing energy down the beam-pipe.*

6.2.1 $e^+e^- \to \gamma\gamma(\gamma)$

The t-channel production of two (or three) hard photons is the only non-negligible source of physics background. Since SiCAL is a calorimeter and not an ionization tracker, photons can not be distinguished from electrons. An event with two collinear high energy photons is then indiscernible from a Bhabha event. Furthermore, the deflection in the ALEPH magnetic field is too small to distinguish photons from electrons with the calorimeter. A $70\,pb^{-1}$ sample of events (corresponding to 8 times the data sample) was produced using the GGG generator [11], in a wide angular region fully containing the SiCAL. Out of the 10000 fully simulated events, corresponding to a cross-section of $0.143\,nb$, only 947 passed the event selection. The total cross-section for the selected events is then $13.6\,pb$ (corresponding to a 0.016% contamination), and was added to the reference Bhabha cross-section (see Sect. 9). The error for this cross-section is estimated using the 3% statistical error from the simulation and assuming a similar contribution for the theoretical error of the generator: the resulting error on luminosity is estimated as 7×10^{-6}.

6.2.2 $e^+e^- \to e^+e^-X$ ("$\gamma\gamma$" interactions)

The contamination was calculated for the $e^+e^- \to e^+e^-X$ reactions ("$\gamma\gamma$" interactions), where two virtual photons radiated by the beam electrons interact and produce either a lepton pair or a hadronic final state, or else resonate into a pseudoscalar meson which then decays giving two real photons. Most of the contamination from this reaction comes from "2-tag" events where both beam electrons recoil from the emitted photon and strike the SiCAL with nearly their full energy. Some minor contamination was also found for those "1-tag" event with a beam electron striking SiCAL in coincidence with some product of the $\gamma\gamma$ interaction. Samples of events of at least $10\,pb^{-1}$ were produced using the PHOT generator for many different final states and for all 2,1 or 0 tag configurations [12, 13]. The hadronic events were generated using both the QED and the VDM modelling of the interaction [14]. The total contamination from these $\gamma\gamma$ events is estimated to be less than 6×10^{-5}, coming from lepton and hadron production. It is not subtracted from the data, but treated as a systematic error.

6.2.3 $e^+e^- \to q\bar{q}$

A $50\,pb^{-1}$ sample of $q\bar{q}$ events was produced using the HVFL generator [15]. The contamination to the Bhabha sample was found to be negligible (less than 5×10^{-6}).

6.2.4 $e^+e^- \to \tau^+\tau^-$

The differential cross-section for $\tau^+\tau^-$ events goes roughly as $(1 + \cos\theta^2)$. Using the peak cross-section value of $2.0\,nb$, the cross-section for generating a τ^- pointing to either SiCAL module within the angular acceptance of the Bhabha selection is $2.5\,pb$. The contamination is estimated conservatively (without applying the standard energy cuts to the products) to be less than 3×10^{-5}.

In summary, only the two hard photon production represents a relevant background contamination to the selected Bhabha sample, and is subtracted. The other sources of physics background as well as the uncertainties in their estimation are covered with a systematic error on luminosity due to physics background of 1.0×10^{-4}.

7 Experimental precision

The experimental uncertainties in the Bhabha cross-section determination come primarily from the precision of the radial fiducial cut, the knowledge of the absolute separation between calorimeters, and the level of understanding shown in the Monte Carlo simulation, including the latter's statistical precision. In most of these areas further improvement with the higher statistics of the 1993 running is expected.

The luminosity experimental systematic errors are summarized in Table 16 (sect. 10). The contributions are described in the following sections.

7.1 Trigger efficiency measurement

The first check of the coincidence trigger uses events which satisfy the single-arm high threshold trigger on one side and which have energy deposits in both calorimeters. The coincidence trigger frequency for such events is plotted versus the energy in the opposite side, shown in Figure 19. The efficiency turn-on is clearly visible at 12 GeV (the low threshold) and full efficiency is reached by 20 GeV.

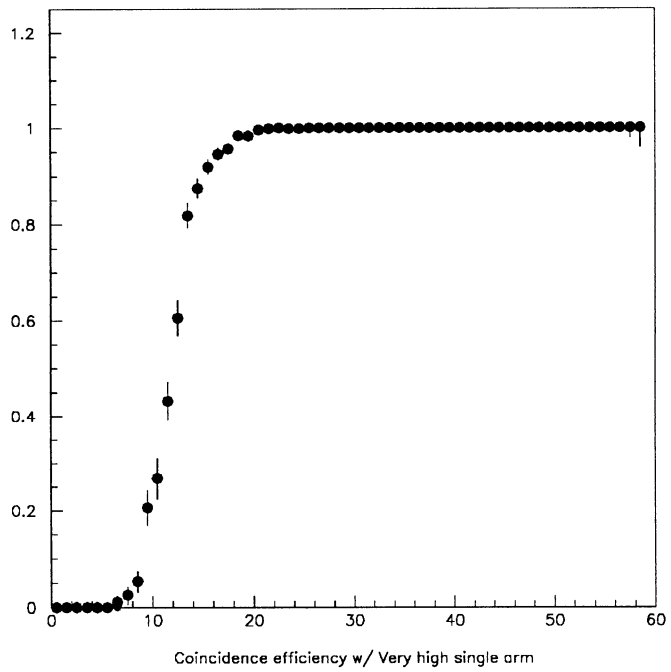

Figure 19: *Efficiency of the the coincidence trigger versus energy on the low side. The very high threshold single arm trigger is used to measure this efficiency.*

A second check uses selected Bhabha events and the independent triggers derived from different sets of planes to verify the efficiency of the coincidence trigger. The Bhabha coincidence trigger derived from the B odd planes and the A even planes, for example, is used to check the efficiency of the same trigger derived from the B even planes and the A odd planes. The inefficiencies of sub-triggers ($A_{odd}\bullet B_{even}$, $A_{even}\bullet B_{odd}$, $A_{odd}\bullet B_{odd}$, $A_{even}\bullet B_{even}$) are all well under 10^{-4}. The Bhabha coincidence trigger is an OR of all these sub-triggers and as such has an efficiency very close to 100%. Comparison with the high single-arm trigger gives a similar result.

During the first weeks after installation, there were problems setting the trigger thresholds uniformly over all segments. Since this introduces correlations into the otherwise independent triggers, the above methods could not be used to measure the efficiency. Instead the low end of the energy spectrum of Bhabha events taken during this period was compared to that of a later period where the detector was functioning properly. No trigger inefficiency was seen in the data taken during this first period. Conservatively, an inefficiency leading to a loss of 1.0×10^{-4} over the data taking period can not be excluded.

7.2 Reconstruction efficiency

The requirement of ≥ 1 reconstructed cluster on each side could introduce losses if the SiCAL event reconstruction failed. No SiCAL coincidence triggered events were rejected by the "number of clusters" selection, for a subsample (250 K coincidence triggers) of the total data set. This gives an upper limit of $1.2\times\ 10^{-5}$ (95 % CL) for the reconstruction inefficiency. Such an effect is then neglible on the cross-section measurement.

7.3 Internal detector geometry precision

The uncertainty on the luminosity coming from a common radial displacement of the inner and outer fiducial cuts (eg. a radial shift of a silicon detector) is given by the following formula :

$$\frac{\delta\mathcal{L}}{\mathcal{L}} = \frac{2\delta R}{R_{min}} \left(\frac{1 - R_{min}^3/R_{max}^3}{1 - R_{min}^2/R_{max}^2} \right). \tag{16}$$

This gives a slightly smaller systematic uncertainty than the displacement of the inner radial cut alone [10]:

$$\frac{\delta\mathcal{L}}{\mathcal{L}} = \frac{2\delta R}{R_{min}}\left(1 + \frac{R_{min}^2}{R_{max}^2 - R_{min}^2}\right). \tag{17}$$

The internal detector geometry discussed in section 2.1 and summarized in Table 2 gives a precision of 18 μm on the radial fiducial cut. Using Eq. 16 and the values for the Bhabha selection cuts: $R_{min} = 7.67\ cm$ and $R_{max} = 12.37\ cm$ yields $\delta\mathcal{L}/\mathcal{L} = 2.47\delta R/R_{min}$, giving a luminosity precision of 5.8×10^{-4}.

7.4 Beam parameters and module positions

One of the advantages of the selection procedure detailed in section 5 is that it makes the acceptance insensitive *in first order* to the exact knowledge of the positions of the modules or of the beam, both along the beam direction as well as transverse to it [16, 17]. The only requirement is that the amount of asymmetry between the fiducial (tight) and non-fiducial (loose) boundaries be larger than the typical size of the beam movements and module misalignments. Specifically, the following condition must be fulfilled:

$$\delta R^{M(m)} > \max\left\{2\Delta x, 2\Delta y, R_{M(m)}\frac{2\Delta z}{z_0}\right\} \tag{18}$$

where $\Delta x, \Delta y, \Delta z$ are the equivalent beam displacements due to real beam effects (displacement or angle) or module misalignments. $R_{M(m)}$ is the maximum (minimum) radius of the acceptance region, z_0 is half the distance between the two opposite calorimeters and $\delta R^{M(m)}$ is the required difference between the outer (inner) radius of the tight and loose sides acceptances.

The values for the final Bhabha selection are $\delta R^m = 10.5$ mm and $\delta R^M = 15.75$ mm. This means that we can tolerate $\Delta x, \Delta y \leq 5$ mm for the radial cuts and $\Delta z \leq 15$ cm without seeing first order effects (that is, effects proportional to $\Delta x/R_m$, $\Delta y/R_m$, $\Delta z/z_0$). All values measured for Δx, Δy, Δz are well within these bounds.

The size of the quadratic effect that remains for this selection has been estimated analytically (due to the simple geometry of SiCAL) and confirmed with the help of a rough Monte Carlo simulation. The resulting change in the number of observed events (and, hence, in the luminosity) is approximately

$$\frac{\Delta\mathcal{L}}{\mathcal{L}} \simeq \frac{7}{4}\left(\frac{\Delta x}{R_m}\right)^2\left(1 + \frac{R_m^2}{R_M^2}\right) \tag{19}$$

for changes in the x direction, with the same definitions as in the previous equation. A similar formula holds for y, while for z reads

$$\frac{\Delta\mathcal{L}}{\mathcal{L}} \simeq 2\left(\frac{\Delta z}{z_0}\right)^2 \tag{20}$$

For the beam angles, Δx is subsituted by $z_0 \cdot \alpha_x$, where α_x is the x component of the angle between the beam line and the line passing through the center of the two SiCAL modules, and similarly for y.

The following task is to determine Δx, Δy, Δz, α_x, α_y. Note that, since only the relative position between SiCAL and the beam is important, those terms can be obtained directly from the data, *without any survey information.* The effective beam displacement Δx can be computed from the knowledge of the beam position (available from other sub-detectors) and the SiCAL position (available from the survey) as

$$\Delta x = \Delta x_{\text{beam}} - \frac{1}{2}\left(\Delta x^A_{\text{SiCAL}} + \Delta x^B_{\text{SiCAL}}\right), \tag{21}$$

can also be obtained simply from the SiCAL data alone as

$$\Delta x = \frac{1}{2}\left\langle x^A_{\text{shower}} + x^B_{\text{shower}}\right\rangle. \tag{22}$$

Similarly, the relative beam angles can be found by:

$$\alpha_x = \alpha_{\text{x-beam}} - \frac{1}{2z_0}\left(\Delta x^A_{\text{SiCAL}} - \Delta x^B_{\text{SiCAL}}\right) \tag{23}$$

or

$$\alpha_x = \frac{1}{4z_0}\left\langle x^A_{\text{shower}} - x^B_{\text{shower}}\right\rangle. \tag{24}$$

and the same procedure is used for the y displacements and angles.

The situation is much less critical for relative z-movements, as can be seen by an inspection of Eq. 20. In this case, the survey data has been used.

During the 1992 running there was an observable shift of a few hundred microns (both in x and in y) in beam positions between the 4-bunch running and the 8-bunch running. In this analysis both periods are averaged. Using the whole of the 1992 data sample the following results for x and y positions and angles are obtained:

$$\begin{aligned} \Delta x &= \frac{1}{2}\left\langle x^A_{\text{shower}} + x^B_{\text{shower}} \right\rangle = -2.1\text{mm} \\ \Delta y &= \frac{1}{2}\left\langle y^A_{\text{shower}} + y^B_{\text{shower}} \right\rangle = 0.2\text{mm} \\ \alpha_x &= \frac{1}{4z_0}\left\langle x^A_{\text{shower}} - x^B_{\text{shower}} \right\rangle = -0.6\text{mrad} \\ \alpha_y &= \frac{1}{4z_0}\left\langle y^A_{\text{shower}} - y^B_{\text{shower}} \right\rangle = 0.2\text{mrad} \end{aligned} \tag{25}$$

These values are used in the Monte Carlo simulation. Differences between data and Monte-Carlo are included in the systematic error. Observable differences can be due to the averaging procedure between 4- and 8-bunch running and to the statistical uncertainties in the parameters determined above (typically considerably smaller than the differences between the 4-and 8-bunch beam positions).

Figure 20 shows that there is an overall good agreement between data and Monte-Carlo for the relevant distributions. Differences between data and Monte-Carlo are around 50 $\pm$ 5 μm for the half-sums of the shower positions and about 300 $\pm$ 100 μm for the half-differences, this last number corresponding to differences around 0.06 ± 0.02 mrad in the beam angles. Since those differences are larger than their uncertainties, they are taken into account in the systematics evaluation. The largest systematic error here comes from α_x and amounts to

$$\frac{\Delta\mathcal{L}}{\mathcal{L}} = \frac{7}{4}\left(\frac{z_0}{R_m}\right)^2\left(1+\left(\frac{R_m}{R_M}\right)^2\right)\left((\alpha_x+\Delta\alpha_x)^2-\alpha_x^2\right) \simeq +2\times 10^{-4}, \tag{26}$$

with $\Delta\alpha_x = +0.06$ mrad. The remaining effects are below 10^{-4}.

Relative movements of the beam tilt during a fill or from fill to fill are monitored by the BOMs (beam orbit monitors). Analysis of the BOM information over the entire running period gives σ_α of 0.13 mrad in x and 0.30 mrad in y. Eq. 26 is used to evaluate the systematic error substituting the last term in brackets by $\sigma_\alpha^2/2$. Using the standard values for R_m, R_M and z_0, it gives $\delta\mathcal{L}/\mathcal{L} = +0.0014 \times \sigma_\alpha^2$, for σ_α in mrad. When including both x and y angle effects, this gives a change in the luminosity of $+1.5 \times 10^{-4}$, which is taken as a systematic error.

The effect of relative z position uncertainty is estimated using the survey measurement as input to the Monte Carlo simulation, where the estimated survey accuracy, 0.5 mm, in Eq. 20, yields a completely negligible uncertainty in $\mathcal{L}$. Possible movements of the beam in the z direction of up to 2 cm (much bigger than expected) would only affect the luminosity below the 10^{-4} level and are, hence, neglected.

Survey measurements show that the large Δx offset was mainly due to a 3.3 mm shift on the A-side of the beam pipe together with the SiCAL A calorimeter. The effect of this offset is clearly visible in the ϕ-distribution shown in Figure 21. The B-side "tight-selection" events' ϕ-distribution shown in the same figure is considerably flatter. The Monte Carlo simulation including the offsets is in good agreement with the data.

Finally, the absolute z-distance between calorimeters directly affects the luminosity by changing the angles of the radial fiducial cut. The knowledge of this distance comes from the survey. A survey precision of 0.5 mm has been assumed. This gives a luminosity precision of 3.5×10^{-4}. As a cross-check of the precision of the survey z-measurements, the data have been used to measure the relative z-distance between calorimeters; the results were compared that with the survey measurement. The z-difference ΔZ can be extracted from the difference between the Side A and Side B mean values of the "loose-side" radial distributions ΔR_{mean}, using the formula:

$$\Delta Z = Z_0\left(\frac{\Delta R_{mean}/2}{2R_0 + \Delta R_{mean}/2}\right) \tag{27}$$

where Z_0 is the mean z for layers 3 and 4 (252.8 cm), R_0 is the "tight-side" mean radius (9.74 cm). The result is $\Delta Z_{data} = 0.46 \pm 0.05\ cm$ which can be compared with the survey determination : $\Delta Z_{survey} = 0.51 \pm 0.03\ cm$. The difference is $0.05 \pm 0.06\ cm$, consistent within the precision of the measurements.

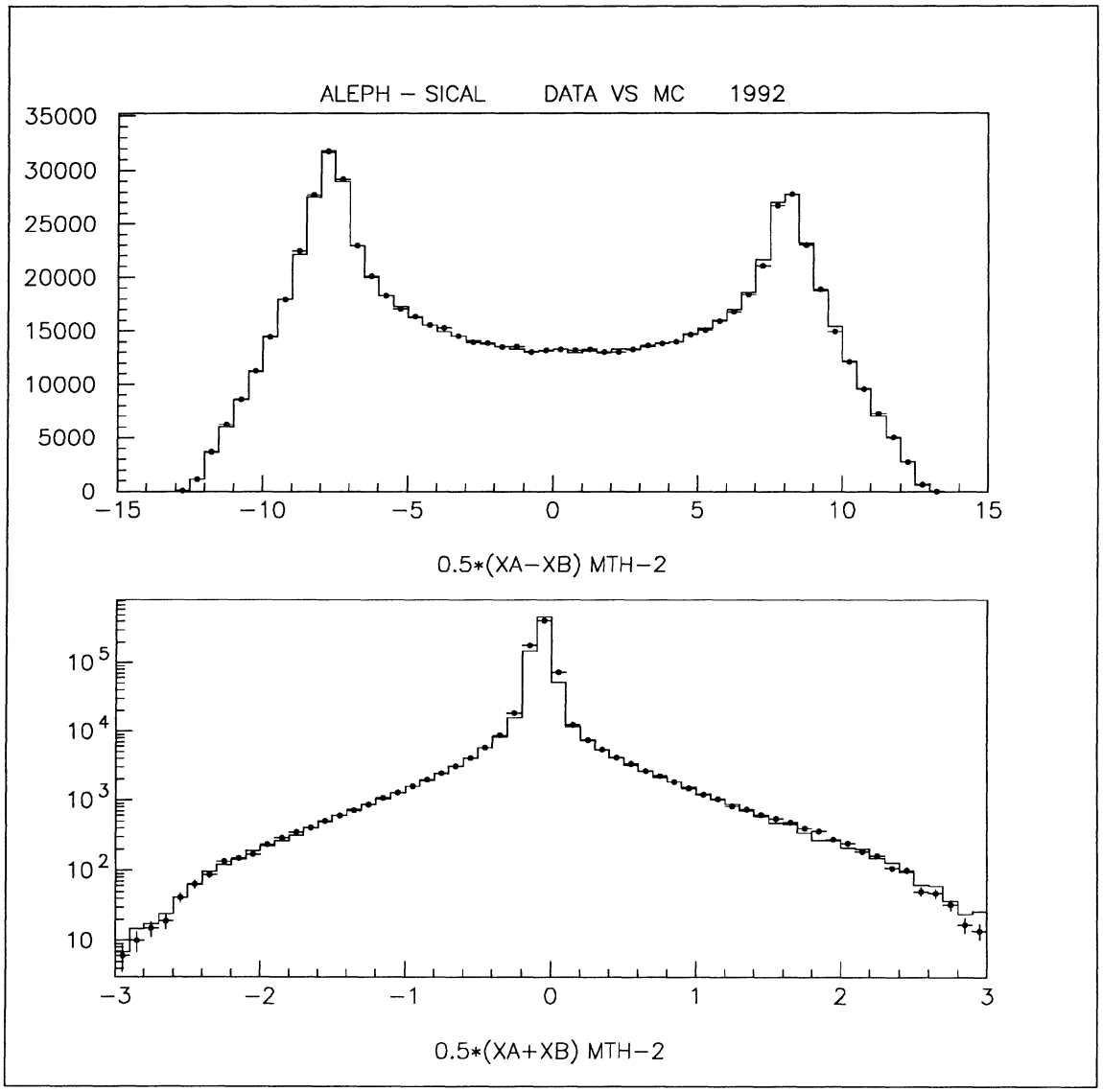

Figure 20: *Top: α_x distribution, $0.5(X_A - X_B)$, and Bottom: Δx distribution, $0.5(X_A + X_B)$, for accepted Bhabha events. The data are plotted as points and the Monte Carlo is shown as a line.*

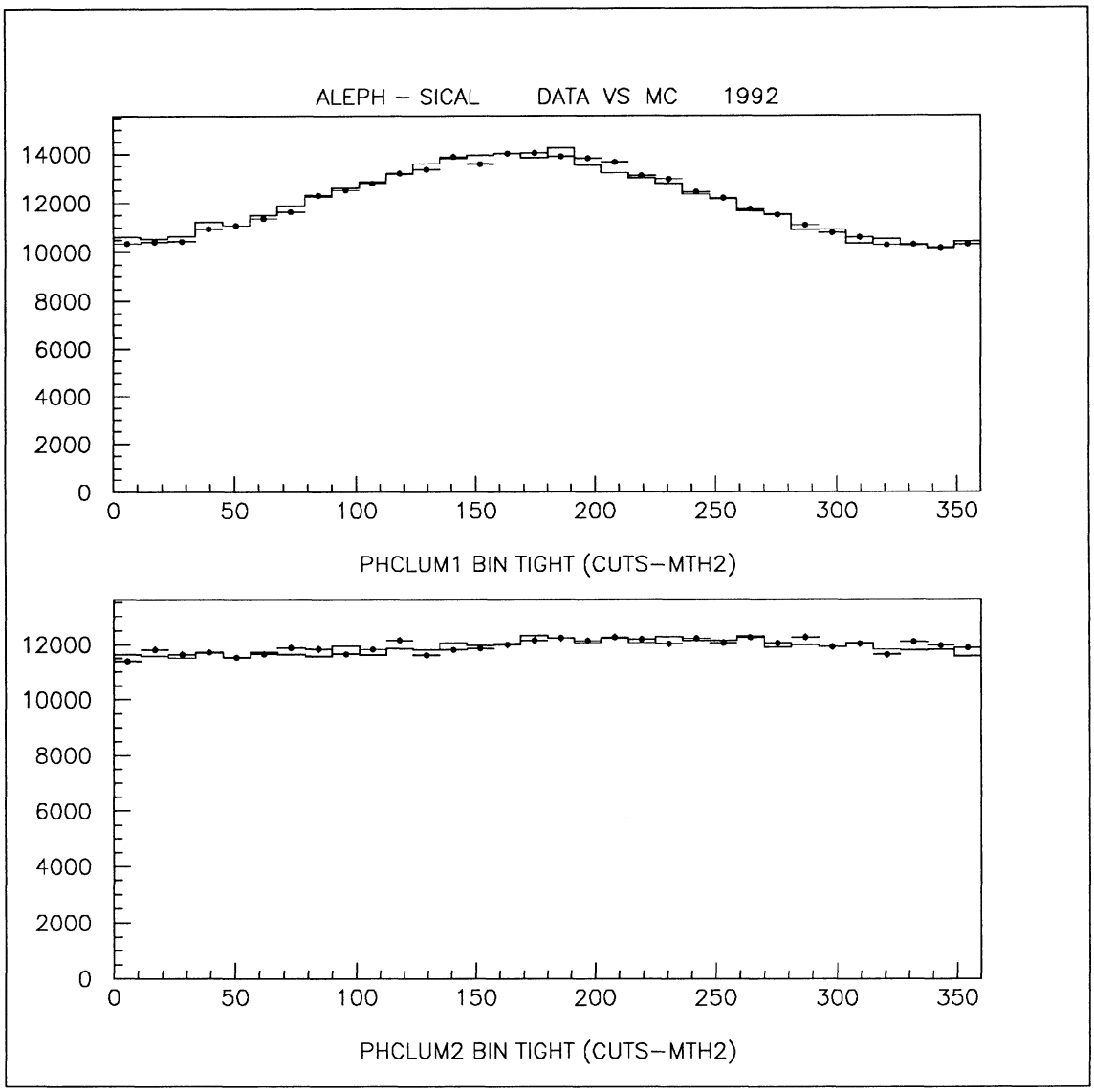

Figure 21: *Top: ϕ distribution for Side-A "tight selection", and Bottom: ϕ distribution for Side-B "tight selection", for accepted Bhabha events. The data are plotted as points and the Monte Carlo is shown as a line.*

7.5 Radial fiducial cut systematic errors

The radial fiducial cut uncertainty comes from two sources: (1) the cell to cell energy calibration and (2) the precision of the electromagnetic shower parametrization used in the Monte Carlo simulation. In addition two other sources could potentially contribute and are included below: (3) material simulation accuracy and (4) inaccurancies in the asymmetry determination for radiative events with two clusters merged together by the clustering algorithm.

The contribution to the radial fiducial cut coming from the cell to cell energy uncertainty δE can be evaluated from the equations used for the internal geometry (Eqns. 16 and 17) using the measurement of dA_r/dR at the pad boundary.

$$\frac{\delta \mathcal{L}}{\mathcal{L}} = \frac{2f}{R_{min}} \left((dA_r/dR)_0^{-1} \delta A_r \right) \tag{28}$$

where $(dA_r/dR)_0$ is the slope at the fiducial boundary, f is the geometrical factor coming from the inner and outer fiducial radii (f = 1.24 for the final Bhabha selection) and $\delta A_r = 1/2\ (\delta E/E)$.

7.5.1 Determination of asymmetry parameters and cell to cell uniformity

The energy asymmetry (ref. Eq. 10 and Figure 12) has been fitted both for the data and Monte Carlo as a function of R_{clus}, the radial cluster barycenter in each layer, with the functional form :

$$A_r = A_o \tanh b\ (R_{clus} - R_{pad} - R_{offset}) \tag{29}$$

where : R_{pad} is the radius at the pad boundary used for the fiducial cut, and R_{offset} is the barycenter radial offset coming from the pad curvature and shower leakage. The fit results are shown for data in Figure 23. The slope flattens as expected as the shower developes in depth.

The parameters which fix the width and relative weight of the 3 gaussian functions used in the shower simulation (see sect. 7.5.3) have been optimized, layer by layer, for the two variables: the slope $dA_r/dR_{clus} = A_o \times b$, at $A_r = 0$, which is critical for the radial fiducial cut, and R_{offset}. This explains the good agreement between the slopes for data and Monte Carlo. The Monte Carlo is then used to extract the true slope at $A_r = 0$, dA_r/dR_{true}, giving a correction for layers 3 and 4 at the inner fiducial cut of

$$(dA_r/dR_{clus})_{DATA} \times \left(\frac{dA_r/dR_{true}}{dA_r/dR_{clus}} \right)_{MC}^{A_r=0} = 5.29\ cm^{-1}. \tag{30}$$

This increase of the slope is in agreement with earlier test beam results.

Although longitudinal or azimuthal gain variations do not affect the fiducial selection, radial gain variations are critical to the asymmetry measurement used to determine the Bhabha acceptance. Radial variations can come from a global systematic effect such as the gain corrections applied in sect. 4.1, or from random pad to pad energy response non-uniformities.

The first uncertainty is easily evaluated using Eq. 28 and the 0.75% gain difference observed at the outer fiducial cut(ref. Table 3). This gives $\delta L/L = 1.4 \times 10^{-4}$.

The second source of systematic error coming from the pad to pad non-uniformity was determined from the data. For each electron or positron, the E_{in} and E_{out} were evaluated in the same way as for the asymmetry cuts (see section 5.3). In order to ensure that the shower was centered near the considered pad boundary (either inner or outer fiducial cut), the sum of the two partial energies was required to be greater than 7 GeV (see Figure 13). The E_{in} and E_{out} peak values were then computed for each of the 32 azimuthal bins in each SiCAL module by fitting a gaussian to the peaks in the distributions (see Figure 22). The effect of the pad to pad energy spread on the asymmetry cut was then taken to be the root mean square of the distribution of

$$\frac{< E_{in} >_i - < E_{out} >_i}{< E_{in} >_i + < E_{out} >_i},$$

where i represents each of the $2 \times 32 = 64$ azimuthal bins. The r.m.s. of the distribution was found to be $\sigma_A = 2.75\%$ at the inner fiducial boundary and $\sigma_A = 3.29\%$ at the outer fiducial boundary. In order to interpret this as a systematic uncertainty in the luminosity, we use Eq. 28, where δA_r is divided by $\sqrt{64}$ to account for the individual bins used for the measurement. This gives $\delta L/L = 2.1 \times 10^{-4}$ (1.6×10^{-4}) at the inner (outer) boundary.

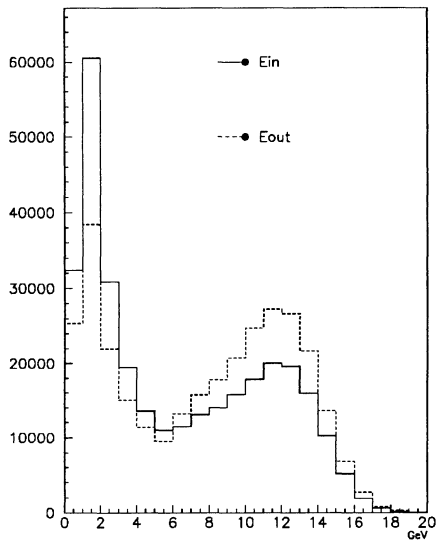

Figure 22: *E_{in} and E_{out} energy distributions for (E_{in} + E_{out}) $\geq$ 7 GeV. E_{in} shown as solid line, E_{out} shown as dashed line. Peak near 12 GeV was fitted with a gaussian to determine variation between pads.*

7.5.2 Evaluation of the "loose-side cut" systematic error

The treatment of the systematic errors follows the method of the tight-side, with the advantage that the radial distribution is flatter at the loose-side boundaries. The loose-side error from the $18\mu m$ uncertainty due to internal geometry (sect. 7.3) is evaluated by considering the event migration for such a displacement of the radial cut with respect to the 5.225 mm padwidth for pad rows 1 and 2 at the inner cut (15 and 16 at the outer cut), see Fig. 15. This gives an error of 3.5×10^{-5}. The pad-to-pad calibration gives an r.m.s. of 5.57% (8.46%) at the inner (outer) loose cut boundary. This is interpreted as a shift of the inner (outer) radial cut of $13\mu m$ ($20\mu m$); the event migration due to this shift yields an error on the luminosity of 3.2×10^{-5} for the inner loose-cut and 1×10^{-5} for the outer cut. A possible systematic shift due to the calibration procedure (see Table 3) is evaluated at 1.5×10^{-5}. Altogether, adding these contributions quadratically gives $\delta\mathcal{L}/\mathcal{L} = 5.1 \times 10^{-5}$.

A more important source of error is the small disagreement between data and the Monte Carlo simulation near the edge of the detector. This is presumably related to poor simulation of shower leakage. The uncertainty is taken into account by varying the loose-side cut from the boundary between pad rows 1 and 2 to the boundary between pad rows 2 and 3. The corresponding change in luminosity (overestimating the effect) gives $\delta\mathcal{L}/\mathcal{L} = 3.2 \times 10^{-4}$.

7.5.3 Shower parametrization and simulation precision

The shower development has been simulated using parametrized distributions in order to reduce the CPU time needed to generate the $O(10^6)$ events sample required for the analysis. The parametrizations were adjusted to the data (as well as previous test beam data) in the central radial region of the detector to avoid energy leakage near the inner or outer edges. In the parametrization the mean value of the "signal" assigned to a pad is proportional to the deposited energy E. The signal is fluctuated according to Poisson statistics, such that $\Delta signal/signal = 24.2\ \%/\sqrt{E}$. The longitudinal development and its fluctuations are treated similarly to the procedure used for ECAL (see ALEPH Handbook, Chapt. IV, sect. 6.4), where the mean profile is given by the formula:

$$\frac{dE}{dS} = (N(E)S^{A(E)-1})e^{-B(E)S} \tag{31}$$

where S is the longitudinal depth in radiation lengths, and N(E) is the energy dependent normalization given by:

$$N(E) = B(E)^{A(E)}E/\Gamma(A(E)). \tag{32}$$

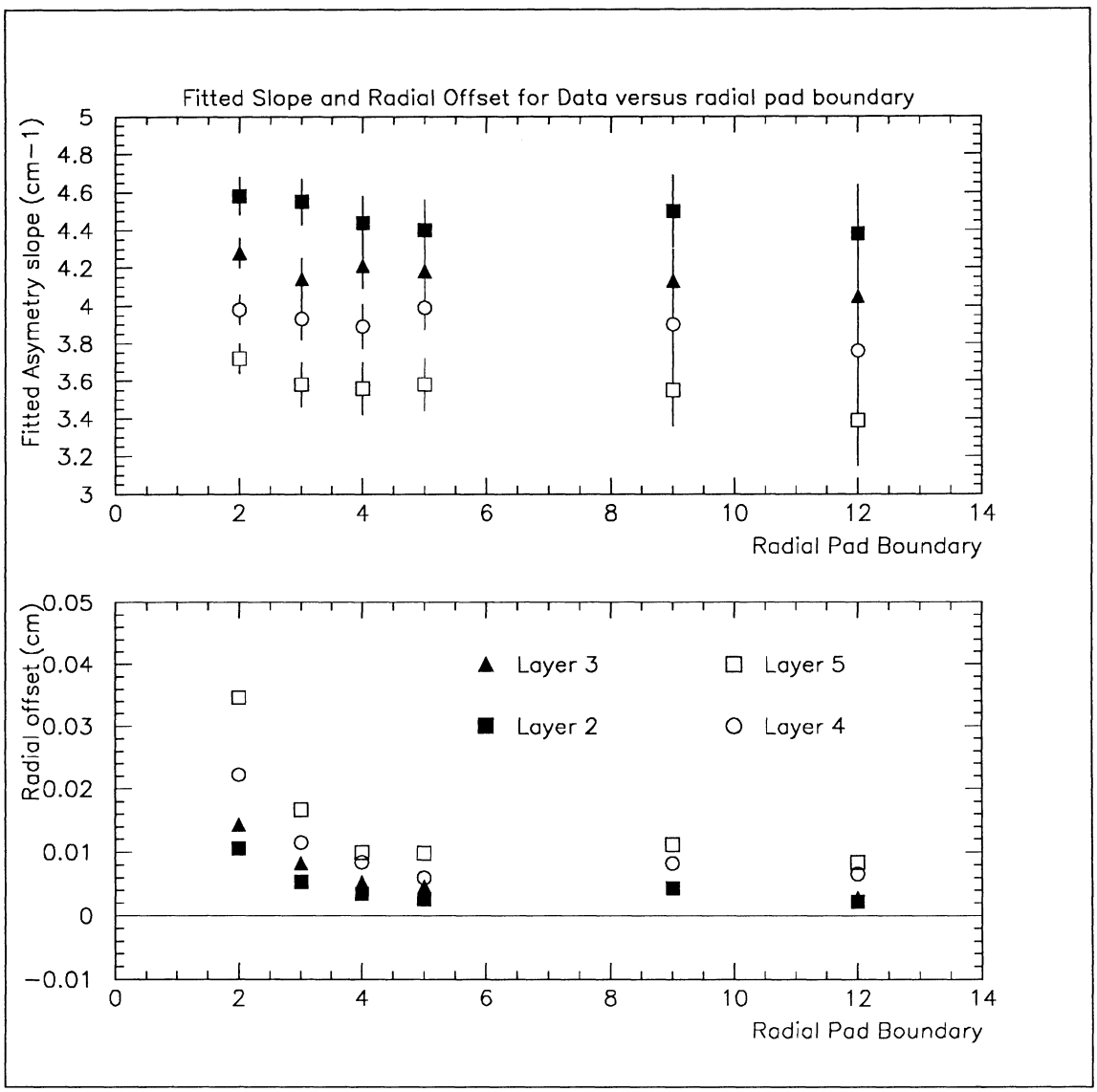

Figure 23: *Fitted slope(above) and radial offset(below) for DATA (layers 2,3,4 and 5) versus radial pad boundary (eg. 2 refers to boundary between pad rows 2 and 3).*

The functions A(E)/B(E) and 1/B(E) were found for ECAL [18] to be well described by linear dependences on the logarithm of the incident energy; the values used were adjusted to SiCAL data:

- E $\geq$ 0.1 GeV:

$$\frac{A(E)}{B(E)} = 5.55 + 1.10 \log E \tag{33}$$

$$\frac{1}{B(E)} = 2.36 - 0.17 \log E \tag{34}$$

- E < 0.1 GeV:

$$\frac{A(E)}{B(E)} = 6.36 + 1.53 \log E \tag{35}$$

$$\frac{1}{B(E)} = 4.31 + 1.07 \log E \tag{36}$$

The longitudinal fluctuations of the showers are simulated by uncorrelated Gaussian smearing of the parameters 1/A and B/A, where:

$$\sigma(1/A) = \sqrt{0.037 + 0.066/E} \tag{37}$$

$$\sigma(B/A) = \sqrt{0.013 + 0.023/E}. \tag{38}$$

Once the deposited energy in each layer is found from the longitudinal distribution, the transverse distribution is used to generate hits (proportional to the energy deposited) randomly over the pads at each depth. The transverse shower distributions themselves were generated from multiple-Gaussian distributions, since the classical $\delta N/\delta x \delta y = A/(r+a)^n$ approach used for ECAL was insufficient to fit simultaneously the dA_r/dR slope, the shower r.m.s. and the shower tail (number of pads/cluster). The shower parametrization has been adjusted to agree with the data's radial distribution since this is critical to the luminosity measurement; furthermore, differences in silicon detector support in ϕ and cross-talk within a detector in R make it difficult to fit simultaneously in R and ϕ. Although a double Gaussian would have been sufficient, three functions were used: historically, dA_r/dR and shower spread were adjusted to the data without regard to the number of pads in the tails using two Gaussians, and a third Gaussian was added to correct for this. Since the shower spread grows as one follows the development into the calorimeter, the Gaussian σ_i^k, (i = 1,2,3), used are defined for each layer k. The values of $\sqrt{2}\sigma_1^k$, $\sqrt{2}\sigma_2^k$ and $\sqrt{2}\sigma_3^k$ and their relative weights 1/(1+2) and (1+2)/(1+2+3) are given in Table 7.

Layer k	$\sqrt{2}\sigma_1$ cm	$\sqrt{2}\sigma_2$ cm	$\sqrt{2}\sigma_3$ cm	1/(1+2) weight	(1+2)/(1+2+3) weight
1	0.16	0.60	0.95	0.800	0.95
2	0.18	0.61	1.00	0.777	0.87
3	0.18	0.59	1.05	0.755	0.85
4	0.18	0.59	1.15	0.662	0.83
5	0.20	0.60	1.20	0.601	0.75
6	0.25	0.65	1.25	0.580	0.70
7	0.25	0.65	1.30	0.473	0.70
8	0.30	0.70	1.40	0.450	0.63
9	0.35	0.75	1.40	0.434	0.60
10	0.41	0.80	1.40	0.405	0.70
11	0.41	0.85	1.40	0.367	0.70
12	0.41	0.81	1.35	0.360	0.70

Table 7: *Electromagnetic shower transverse distribution parametrization: widths and relative weights of the three Gaussian distributions fitted to the data versus depth.*

Because of the pad curvature, the energy asymmetry will be non-zero at the pad boundary: an electromagnetic shower will give more energy to the pad at larger radius. The effect scales with the inverse square of the radius. The Monte Carlo simulation was used to study the radial offset as a function of the shower parameters. The offset

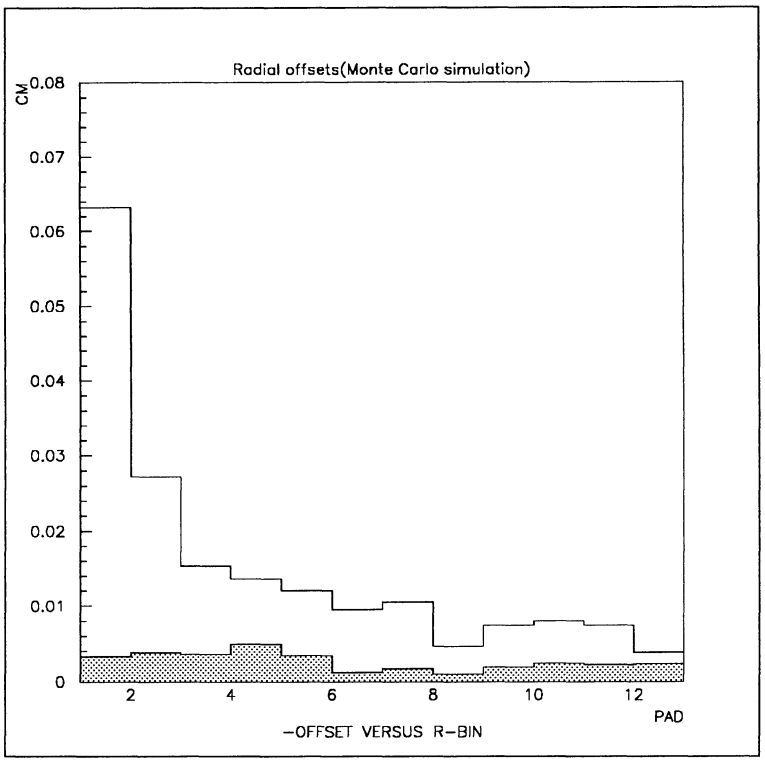

Figure 24: *Monte Carlo simulation radial offsets versus radial bin (not evaluated above bin 12). The asymmetry offset (hashed) is small and varies slowly across the acceptance, whereas the barycenter offset is large and is sensitive to leakage at radii near the edge of the detector.*

is found to be 28 $\pm$ 4 μm and, furthermore, remains stable within 7 μm for variations of the parameters well outside the limits of the measured transverse profile. The resulting uncertainty on the luminosity is 2.3×10^{-4}.

A second "offset" which affects only the cluster radial barycenter, and thus the measured radial distributions, but not the luminosity selection, is due to the edge losses from the finite detector size. This term varies from > 600 μm at small radii down to ≤ 100 μm at the outer fiducial cut. The relative importance of both offsets can be seen clearly in Figure 24. Such a contribution would directly affect a luminosity selection based upon a "barycenter" method rather than A_r.

The non-projective geometry of the silicon pads can introduce some systematic radial shift between data and Monte Carlo for the offset of the asymmetry at the pad boundary due to differences in the longitudinal shower profile. This effect, proportional to the incident shower angle, was minimized by summing over only two layers in depth ($\Delta Z = 1.006$ cm) when evaluating the energies E_{in} and E_{out} used in the asymmetry selection. Figure 25 shows the longitudinal profile for events near the inner fiducial cut. The luminosity uncertainty coming from this source was evaluated using the formula:

$$\frac{\delta \mathcal{L}}{\mathcal{L}} \cong \frac{2\Delta Z}{Z_{clus}} \left(\frac{\delta(E_3/E_4)}{(1 + E_3/E_4)^2} \right) \tag{39}$$

where E_3 and E_4 are the layer 3 and layer 4 energies, and $\delta(E_3/E_4)$ repesents the shift between data and Monte Carlo for these layers. The small disagreement between data and Monte Carlo gives an uncertainty $\delta\mathcal{L}/\mathcal{L} = 2.5 \times 10^{-5}$.

7.5.4 Material simulation accuracy

A potential source of systematic error is the accuracy of the simulation of the material in front of SiCAL. Particles entering the calorimeter must traverse the aluminum beam-pipe at small angles (24 to 58 mrad) and pass through the SAMBA background monitor ($\simeq$ 2% Xo), shown in Figure 26. Typically, the total thickness varies smoothly from 54% Xo at 28 mrad (inner fiducial cut) down to 34% Xo at 48 mrad (outer fiducal cut), excepting locally for two beam-pipe support rings ($\simeq$ 12% Xo). A poor description of this material could produce a systematic shift in A_r(R). In addition, the parametrization assumes the full incident energy is carried to the SiCAL front face before

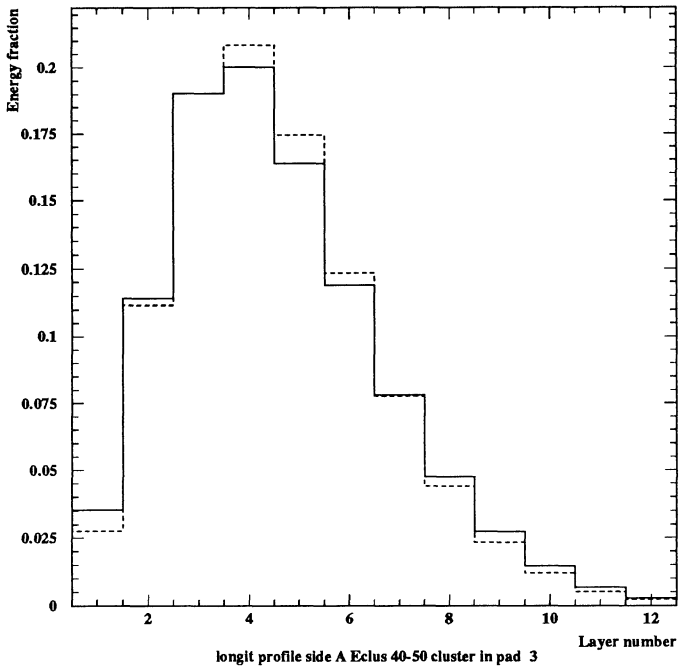

Figure 25: *Shower profile for events centered in radial pad 3 and with* $40 \leq E_{clus} \leq 50$ *GeV. Data are shown as a solid line and the Monte Carlo is shown as a dashed line. ("Tight-side" fiducial cut based upon layers 3 and 4).*

showering, whereas most electrons will have begun showering in the beam pipe. The effect of the B-field on the lower energy particles traversing to the SiCAL face has been estimated to produce a neglible radial shift of the barycenter.

A study of the longitudinal shower profile versus incident angle permits a cross-check of the material used in the Monte Carlo simulation. Figure 27 shows good agreement between data and Monte Carlo in the region of the fiducial cuts. The inner beam-pipe support ring is clearly visible on the B-side. The systematic uncertainty on the simulation of the shower distribution due to the material description is assumed to be negligible.

7.5.5 Cluster barycenter effects on asymmetry determination

A potential source of bias for radiative Bhabha events could come from the cluster radial barycenter used to select the range of pads used in the asymmetry cut (described in section 5.3). Such a problem could occur when an electron (or positron) and the radiated photon are close enough to be confused as a single shower but far enough apart that the barycenter is somewhere between them. In such cases the pad energies used for the A_r calculation could be quite low and subject to fluctuations.

In order to evaluate this effect an alternative algorithm was developed. Instead of starting from the cluster barycenter, the pad row with the cluster's highest energy fraction is used; the event is kept if this pad row is inside the fiducial region. All events failing one but not both selections were scanned: all were identified as "radiative Bhabhas". The overall difference between data and Monte Carlo for the two approaches gives $\delta\mathcal{L}/\mathcal{L} = 5 \times 10^{-5}$ which we take as a conservative systematic error for the method.

7.6 Systematic uncertainty from energy cuts

The larger width of the energy distribution of selected Bhabhas for the Monte Carlo with respect to the data is presumably due to excess shower leakage in the Monte Carlo brought on by the large width Gaussian used in the shower parametrization. In addition, the overall calibration factors in data and in Monte Carlo were obtained in an *ad hoc* fashion in order to obtain a Bhabha peak at the center of mass energy. As a result of these two effects,

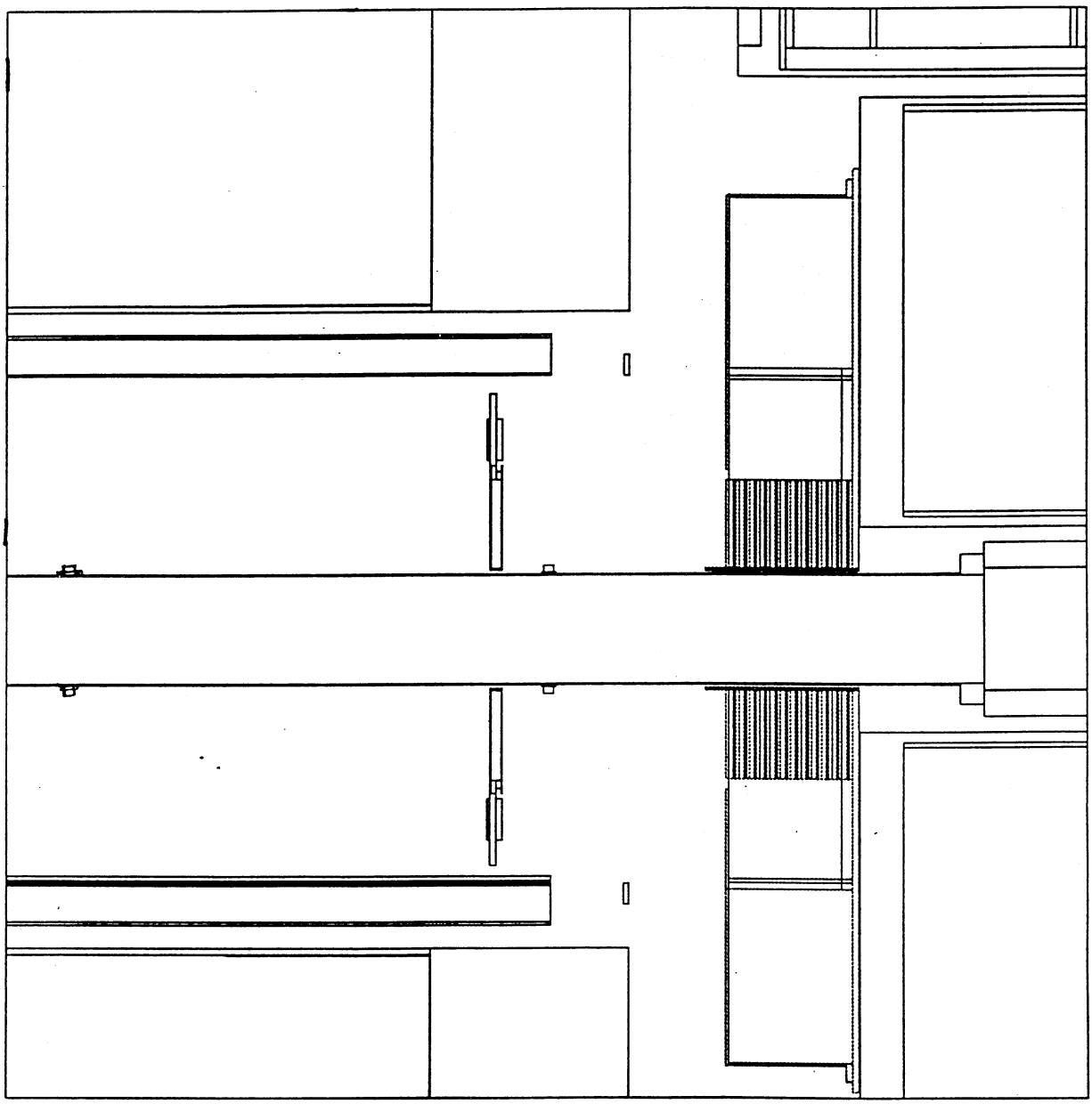

Figure 26: *Section y-z view of the ALEPH forward inner detector region. Bhabha electrons/positrons must traverse the 1.5 mm thick aluminum beam pipe and the SAMBA background monitor ($\simeq$ 2 % X_0) before entering SiCAL.*

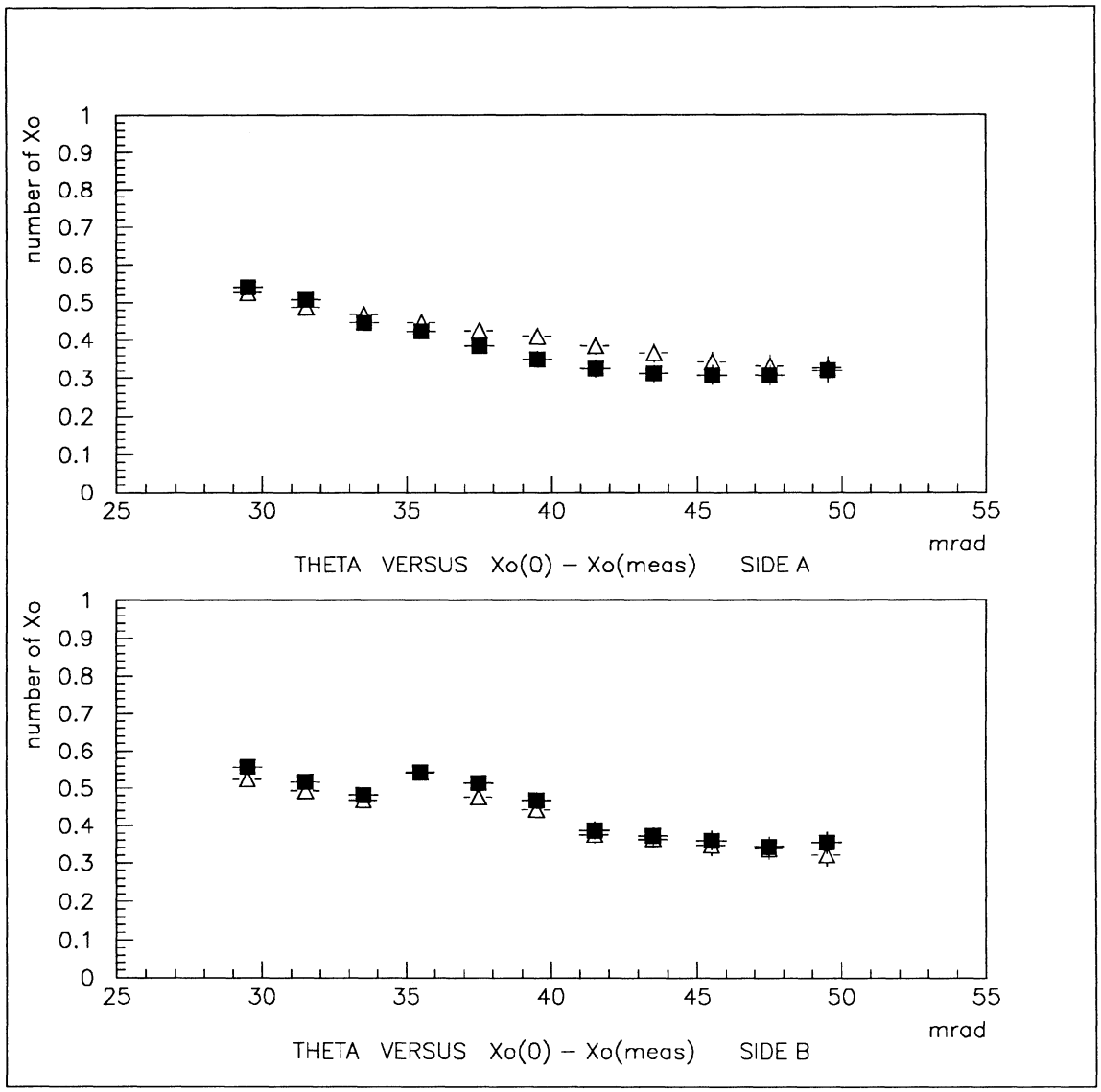

Figure 27: *Difference in shower depth (normal incidence - measured) plotted versus θ. The inner beam-pipe support ring missing in the upper figure (Side A) was removed for VDET installation. Data are shown as full squares and the Monte Carlo simulation as open triangles.*

the single arm energy cut at 20 GeV is $.47\sigma \approx 1$GeV further from the peak in data than in Monte Carlo. Varying the single arm energy cut by 1 GeV produces a change in acceptance of $.9 \times 10^{-4}$ on the fiducial side and 1.1×10^{-4} on the loose side. By similar arguments, varying the total energy cut by 2 GeV produces a change in acceptance of $.5 \times 10^{-4}$, after the 20 GeV cut on each arm is applied. The total systematic error due to energy cuts is taken to be the sum of these three components in quadrature, or 1.5×10^{-4}. Because there may be some correlation between events lost due to the energy cuts when they are near the edge of the geometrical acceptance, it is conservative to add the contributions in quadrature.

7.7 Systematic uncertainty from acoplanarity cut

In order to study the effect on $\Delta\phi$ of the gain corrections made for each ϕ bin, the ϕ of each cluster was reconstructed with and without the gain corrections. Figure 28 shows the difference between the two estimates of ϕ as a function of ϕ for each SiCAL module, and the difference between the two estimates of $\Delta\phi$. It can be seen that the variation is typically less than 0.2°, except for the region in SiCAL A in which a large correction was made for a crystal with low gain in layer six. In all cases the variation is less than 1°. Therefore an upper limit on the systematic uncertainty from this source of $\delta L/L = 5 \times 10^{-5}$ was estimated from the change in acceptance due to changing the $\Delta\phi$ cut by one degree.

7.8 Selection cross-checks

Three cross-checks are used to verify the quality of the final selection, referred to as "Method 2":

1. Loosened radial fiducial cut ("Method 1"), used to study parametrization fidelity.
2. ϕ selections ("vertical" and "horizontal"), used to check for possible systematic effects which might create differences in the treatment of events in the vertical versus horizontal planes (eg. background subtraction residuals or possible errors in the separation between half-modules). These selections are subsets of Method 1 and 2.
3. Stability of selected events with respect to hadronic events, used to check global efficiency.

Comparisons of data and Monte Carlo for ratios of luminosity selections for checks (1) and (2) are shown in Table 10, where the radial fiducial cuts are defined in Table 8 and the "vertical" and "horizontal" ϕ selections are defined in Table 9. The agreement between data and Monte Carlo is within the statistical precision.

SELECTION	Tight Side			Loose Side		
	iR_{min}	iR_{max}	ϕ	iR_{min}	iR_{max}	ϕ
Method 1	3	12	all ϕ	2	15	all ϕ
Method 2	4	12	all ϕ	2	15	all ϕ
Method 3	3	12	"vertical"	2	15	all ϕ
Method 4	3	12	"horizontal"	2	15	all ϕ
Method 5	4	12	"vertical"	2	15	all ϕ
Method 6	4	12	"horizontal"	2	15	all ϕ

Table 8: *Luminosity method fiducial cuts. "Method 2" is the final luminosity selection, other methods are used as cross-checks. Radial pad limits are inclusive, ϕ selections "vertical" and "horizontal" are discussed in the following table.*

The cross-check of the stability of the luminosity selection (3) can be seen in Figure 29 where the ratio of Bhabhas (background subtracted) to TPC-selected hadrons is plotted versus fill number. The ratio is constant within the statistical precision of the points.

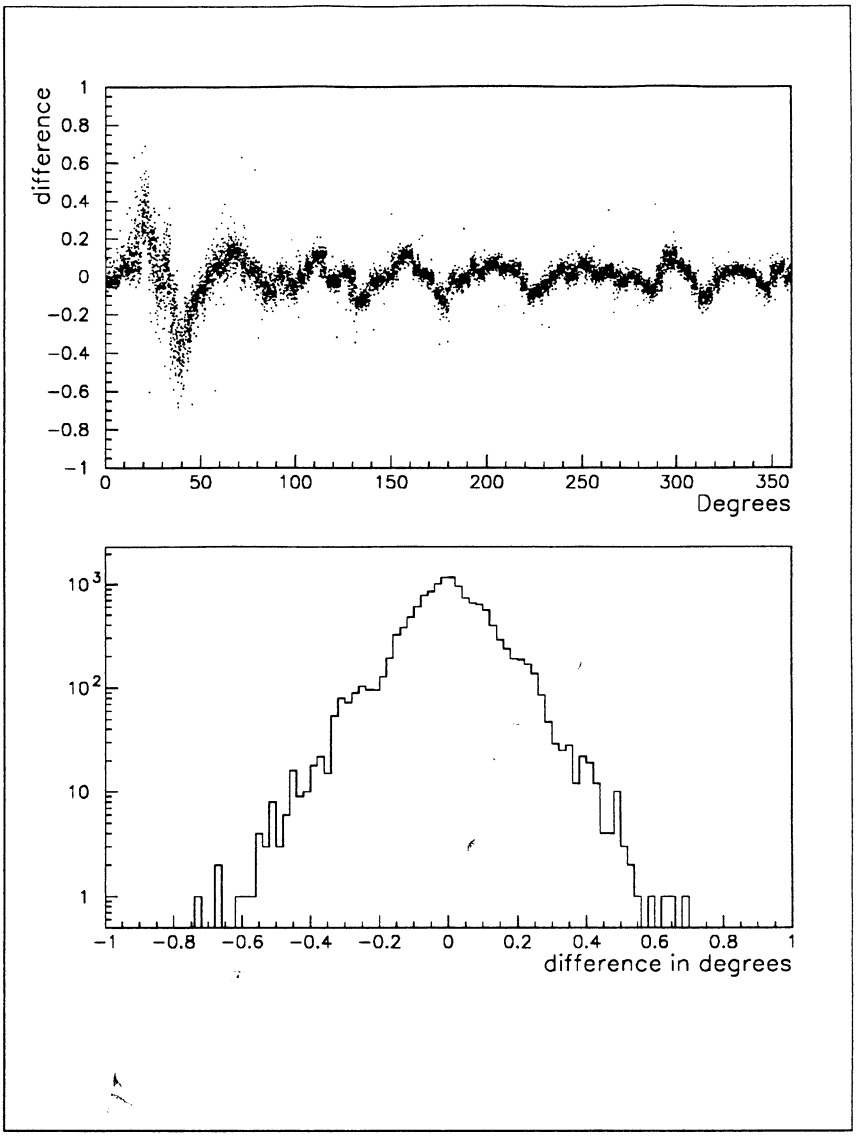

Figure 28: *Top:* $\phi_{gaincorrected}$ - $\phi_{uncorrected}$ *difference for Side A clusters. Bottom:* $\Delta\phi_{gaincorrected}$ - $\Delta\phi_{uncorrected}$ *difference.*

SELECTION	METHOD 1	METHOD 2	ϕ_{low} to ϕ_{high}	ϕ_{low} to ϕ_{high}
"Vertical"	3	5	56.25° – 123.75°	236.25° – 303.75°
"Horizontal"	4	6	326.25° – 33.75°	146.25° – 213.75°

Table 9: *Luminosity method cross-checks: ϕ acceptance for "vertical" and "horizontal" selections in either band [ϕ_{low} – ϕ_{high}]. Selections 3 and 4 are subsets of "Method 1" radial cuts, and 5 and 6 are subsets of the "Method 2" selection.*

Luminosity cross-checks	Data-background	Monte Carlo
Method 1 / Method 2 : opened R cut / standard cuts	1.237±0.001	1.238±0.001
Method 4 / Method 3 : horizontal lumi / vertical lumi	1.001±0.002	1.004±0.003
Method 6 / Method 5 : horizontal lumi / vertical lumi	1.003±0.003	1.006±0.003

Table 10: *Luminosity method cross-checks: ratio of methods compared for data (background corrected) and Monte Carlo (errors shown are only statistical). Methods 3 and 4 are based upon the opened R cut ("Method 1"), whereas methods 5 and 6 are based upon the standard cuts ("Method 2").*

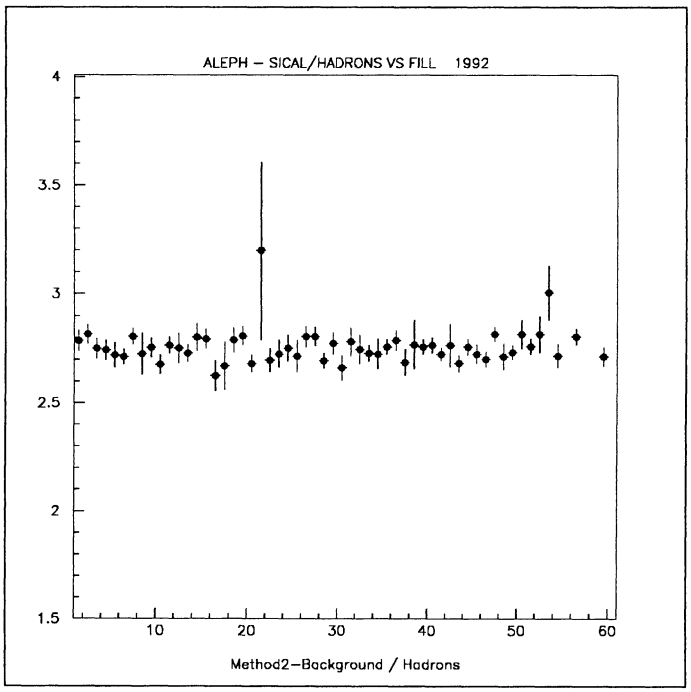

Figure 29: *Ratio of background corrected Bhabhas to hadronic events (TPC and calorimeter selections averaged), plotted versus fill number.*

8 Bhabha cross-section

8.1 BHLUMI generation

The raw kinematics generation of the low angle Bhabha events has been done using the BHLUMI Monte Carlo generator [21]. In this generator, complete $\mathcal{O}(\alpha)$ QED corrections are included together with multiphoton production following the Yennie-Frautschi-Suura scheme [22].

The generation ($\approx$ 9 million generated events) is done in a very loose angular range, 0.6° (10.5 mrad) to 4.1° (71.6 mrad), corresponding to a 1149.49 nb cross-section, and is followed by a preselection based on kinematical quantities of the energy that the produced event will deposit in SiCAL. If this energy is larger than 0.5 GeV in two enlarged regions around both SiCAL sides, the event is kept for tracking into the detector simulation package. Roughly 2 million events pass this preselection, corresponding to a cross-section of 253.738 $\pm$ 0.168 nb.

In addition, the combined beam position offsets, angles (see sect. 7.4) and vertex smearing were introduced to reflect the observed values from the data. They are summarized in Table 11.

Offset	X-position	Y-position	Z-position
	-0.21 cm	0.02 cm	0.0 cm
Beam angles	α_x	α_y	
	-0.59 mrad	+0.20 mrad	
Smearing	σ_x	σ_y	σ_z
	0.014 cm	0.0010 cm	1.00 cm

Table 11: *Summary of beam offsets, angles and vertex position smearing used in BHLUMI generation.*

8.2 GALEPH production

The full Monte-Carlo simulation to determine the cross-section of Bhabha events within the acceptance cuts was performed in the following way: the roughly 2 million BHLUMI preselected events were sent through the full detector simulation program (GALEPH) in order to produce the raw data digitizings and simulate the trigger. The full geometry was described, including the geometrical offsets along the beam of the two calorimeters. The detailed internal alignment was used to deposit energy in the pads. Energy deposition in SiCAL was simulated using a parametrized shower generator.

The simulated "data" were reconstructed using the same program as the real data (JULIA), including dead pads and the more detailed geometry (internal alignments and survey measurements). The reconstructed Monte Carlo "data" passed the same event selection as the data. Table 12 summarizes the generated events and the accepted cross-sections for the different selections. Altogether 668 254 events passed the final luminosity selection giving a BHLUMI cross-section of 84.108 $\pm$ 0.101 nb. The Monte Carlo statistical precision is 0.120 %. The BHLUMI cross-section lacks the electroweak correction which is described in the next section.

8.3 Z-exchange electroweak corrections

Although BHLUMI describes the t-channel photon contribution with good precision, it includes only the Born approximation s-channel Z-exchange. This is considered sufficient for the event simulation, however the final cross-section must be corrected for the missing terms. The procedure used by W. Beenakker and B. Pietrzyk [19, 20] corrects the BHLUMI cross-section for full $\mathcal{O}(\alpha)$ Z-exchange with the BABAMC generator [23]. Using a high-statistics "fast" simulation which includes the SiCAL cuts on kinematical quantities, they have evaluated the electroweak contribution from BABAMC. Comparing the results from a similar run using BHLUMI under the same conditions gives the correction to the final cross-section. Figure 30 shows the size of the Z-exchange Born + $\mathcal{O}(\alpha)$ corrections for both SiCAL and LCAL acceptances versus $\sqrt{s}$ (GeV). The importance of the Z-exchange is 4$\times$ lower in the SiCAL acceptance with respect to LCAL since the SiCAL fiducial region is at smaller angles. The difference in the Z-exchange terms between BHLUMI and BABAMC generations at 91.268 GeV selected for the SiCAL acceptance gives a cross-section correction of + 0.061 % (applied in section 9).

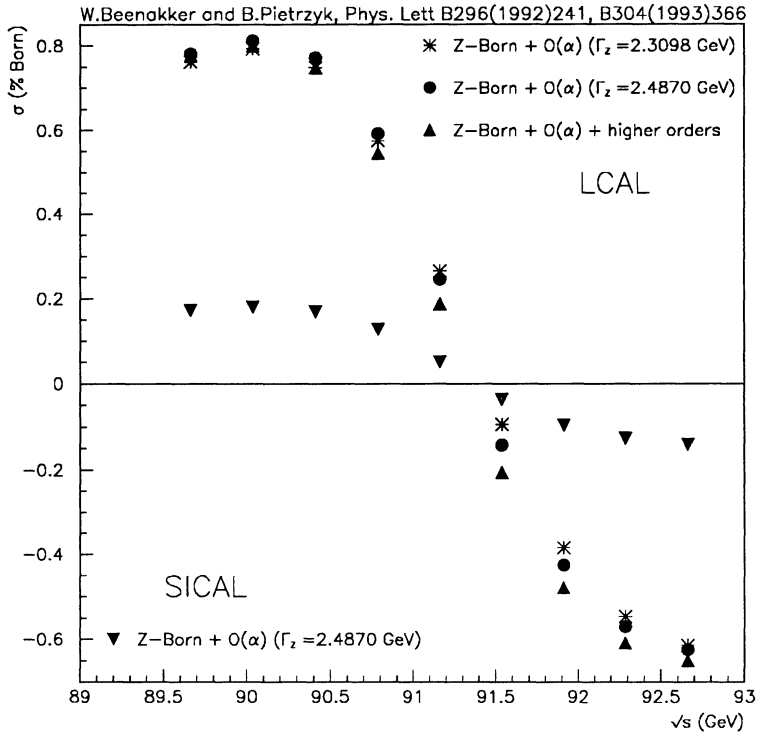

Figure 30: *Z-exchange Born + $\mathcal{O}(\alpha)$ electroweak contribution to the Bhabha cross-section shown for SiCAL and LCAL acceptances (W. Beenakker and B. Pietrzyk).*

8.4 Theoretical systematic error

The evaluation of the theoretical uncertainty in the Bhabha cross-section determination using the SiCAL selection was done by W. Beenakker and B. Pietzyrk (ref. [20] cited above). The luminosity theoretical systematic errors are summarized in Table 13. A brief discussion of their approach is given below and in the three following subsections.

Altogether five programs were used by them to evaluate the uncertainties; QED terms used (see Table 14) include LL(leading-log) and SL(sub-leading): either NL(non-leading) or NLL(next to leading log), where the typical large logarithm used is

$$L = \ln \frac{|t|}{m_e^2} \tag{40}$$

and t is the usual square of the momentum transfer

$$t = -\frac{s}{2}(1 - \cos\theta). \tag{41}$$

- OLDBIS [25] : complete QED $\mathcal{O}(\alpha)$ generator.
- BABAMC [23] : complete electroweak $\mathcal{O}(\alpha)$ photon and Z exchange, including interference terms.
- ALIBABA [24] : semi-analytic program containing LL terms to $\mathcal{O}(\alpha^2)$ and NL terms to $\mathcal{O}(\alpha)$, includes Z-exchange contribution.
- LUMLOG [26] : includes exponentiated LL intial-state corrections up to $\mathcal{O}(\alpha^3)$ for photon t-channel (no NL and NNL terms).

- BHLUMI [21] : Multiphoton generator (Y.F.S. scheme ref. [22]) including $\mathcal{O}(\alpha)$ t-channel photon exchange and Born level Z s-channel exchange, including interference.

Basically, the different generators were compared in common regions, for example, by "switching-off" the weak correction when studying the t-channel contribution. Two types of precision were addressed:

- "Technical precision" : includes soft photon k_o cutoff choice, integration approximations, Monte Carlo implementation details (quasi-random numbers) and eventually programming "bugs".
- "Physical precision" : includes missing higher order terms.

8.4.1 t-channel photon precision

Although the Bhabha cross-section is dominated by the Born t-channel photon exchange, $\mathcal{O}(\alpha)$ LL corrections are around 5 % of this and $\mathcal{O}(\alpha^2)$ LL corrections can be as much as 0.3 to 0.8 %. It is therefore necessary to verify the generator to this level. BHLUMI was checked by using the OLDBIS program for the $\mathcal{O}(\alpha)$ and the LUMLOG program for $\mathcal{O}(\alpha)$ LL and $\mathcal{O}(\alpha^2)$ LL corrections, both programs have technical precisions of 0.02 %. BHLUMI and OLDBIS + LUMLOG were found to agree to within 0.15 %. (Recent work indicates that the disagreement at this level is due to the physical, and not technical, precision of BHLUMI [ref. S. Jadach, private communication]). The $\mathcal{O}(\alpha^2)$ SL uncertainty in BHLUMI was evaluated in reference [21] and is estimated to be 0.09 %, limited by physical precision.

8.4.2 Electroweak corrections

The Z-exchange contribution (ref. Figure 30) varies across the peak due to the interference term $(Z_s - \gamma_t)$ with a maximum value of | 0.2 % | of the Born cross-section. As discussed in section 8.3 the size of this correction was evaluated using the BABAMC program. ALIBABA was used to check this result. The $\mathcal{O}(\alpha)$ Z-exchange comparison agreed to 0.03 % (technical precision) for the interference correction. BABAMC does not include higher order Z-exchange terms, thus the uncertainty on missing terms was evaluated from ALIBABA. The $\mathcal{O}(\alpha^2)$ LL contribution was found to be 0.015 % from ALIBABA and is used as the error for BABAMC. The $\mathcal{O}(\alpha^2)$ SL terms which are not included in ALIBABA were conservatively estimated to be as large as the LL terms.

8.4.3 Vacuum polarization

The vaccum polarization is assumed to be the dominant non-QED correction to the t-channel photon-exchange. It is included in BHLUMI and represents a total correction of 3.96 %. Although the main part of the correction comes from the leptonic loops which are well understood, the largest source of uncertainty is the hadronic contribution to the vacuum polarization (roughly 30 % of the total). The hadronic part has been studied by evaluating a dispersion integral over the measured $e^+ e^- \rightarrow$ *hadrons* ref. [27], and has a relative uncertainty of 4.5 % within the t-range covered by SiCAL. The uncertainty on the vacuum polarization was thus estimated to be 0.05 %

As an additional check, the authors of ref. [20] compared the implementation of the correction in BABAMC (which simply adds an $\mathcal{O}(\alpha)$ correction of 2 Re$\prod$ = 4.01 %) with ALIBABA and found them coherent to 0.01 % The BHLUMI treatment is considered equivalent and agrees at the 0.02 % level.

	Number Generated	Number Accepted	σ_{Acc} nb	error nb
BHLUMI Gen		9132931	1149.490	±0.263
Preselection	9132931	2016000	253.738	±0.168
GALEPH	2016000	see below		
SELECTION				
Method 1	2016000	827469	104.147	± 0.112
Method 2	2016000	668254	84.108	± 0.101
Method 3	2016000	309427	38.945	± 0.069
Method 4	2016000	310618	39.095	± 0.070
Method 5	2016000	249668	31.424	± 0.062
Method 6	2016000	251150	31.610	± 0.063

Table 12: *Summary of generated events and accepted cross-sections. About* 66% *of the final BHLUMI "preselected" events* ($\sigma_{Acc} = 253.738$ *nb) give SiCAL coincidence triggers.*

(1) $\mathcal{O}(\alpha^2)$ LL BHLUMI	0.15%
(2) $\mathcal{O}(\alpha^2)$ SL BHLUMI	0.09%
(3) Z-exchange $\mathcal{O}(\alpha)$ BABAMC	0.03%
(4) Z-exchange $\mathcal{O}(\alpha^2)$ missing LL BABAMC	0.015%
(5) Z-exchange $\mathcal{O}(\alpha^2)$ missing SL BABAMC	0.015%
(6) Vacuum polarization	0.05%
TOTAL theoretical uncertainty	0.25%

Table 13: *Summary of luminosity measurement theoretical systematic errors. Leading-log (LL) and sub-leading (SL) uncertainties for the photon-exchange (1 and 2) and Z-exchange (4 and 5) are each added linearly. (W. Beenakker and B. Pietrzyk).*

Order	Leading terms	Sub-leading terms	
0	Born - - - - - - - - - - BABAMC, ALIBABA BHLUMI OLDBIS(QED), LUMLOG(QED)		
1	(α/π)L LL $\mathcal{O}(\alpha)$ - - - - - - - - - - BABAMC, ALIBABA OLDBIS(QED), BHLUMI(QED) LUMLOG(QED)	(α/π) NL $\mathcal{O}(\alpha)$ - - - - - - - - - - BABAMC, ALIBABA OLDBIS(QED), BHLUMI(QED)	
2	$(\alpha/\pi)^2L^2$ LL $\mathcal{O}(\alpha^2)$ - - - - - - - - - - ALIBABA, LUMLOG(QED) [BHLUMI(QED)]	$(\alpha/\pi)^2$L NLL $\mathcal{O}(\alpha^2)$ - - - - - - - - - - [BHLUMI(QED)]	$(\alpha/\pi)^2$ SL $\mathcal{O}(\alpha^2)$
3	$(\alpha/\pi)^3L^3$ LL $\mathcal{O}(\alpha^3)$ - - - - - - - - - - LUMLOG(QED) [BHLUMI(QED)]	$(\alpha/\pi)^3L^2$ NLL $\mathcal{O}(\alpha^3)$	$(\alpha/\pi)^3L$ SL $\mathcal{O}(\alpha^3)$

Table 14: *QED classification of terms containing logarithms in Monte Carlo event generators. Generators are full electroweak except where (QED) is noted: γ-exchanges only. BHLUMI in [ ] gives partial contribution due to exponentiation.*

9 Final corrected cross-section and 1992-SiCAL integrated luminosity

The accepted BHLUMI cross-section (ref. section 8.2) for the "Method 2" selection : $\sigma_{SiCAL} = 84.11 \pm 0.10\ nb$, must be corrected for the t-channel two hard-photon background, + 0.015 % (ref. section 6.2.1), and the missing Z-exchange contributions, + 0.061 % (ref. section 8.3). This yields :

$$\sigma^{corr}_{SiCAL} = 84.17 \pm 0.10\ nb \tag{42}$$

The integrated luminosity is given by :

$$\int \mathcal{L}\ dt = \frac{N_{Bhabha}}{\sigma^{corr}_{SiCAL}} \tag{43}$$

where $N_{Bhabha} = N_{data} - N_{background}$, the number of events passing the luminosity selection cuts, background subtracted.

The SiCAL luminosity for 1992 "electroweak selection" is evaluated for runs with SLUMOK (high voltage bits on and trigger enabled) and XLUMOK. Essentially 95.5 % of runs taken since the detector installation, starting from 16674 upwards to 17864, were used (57 LEP fills). Runs removed for various reasons are summarized in Table 15. Altogether $\simeq 10^6$ SiCAL triggers were processed, yielding (after JULIA reconstruction and luminosity selection) for the two-month period:

$$737042\ \textit{Selected events} - 639\ \textit{background events} = 736403\ \textit{Bhabhas}. \tag{44}$$

Runs rejected	Luminosity lost	Comments
16648 to 16673	190 nb^{-1}	SiCAL "hold" timing adjustments
16764 to 16767	30 nb^{-1}	SiCAL out of DAQ partition
16680 to 16682	30 nb^{-1}	no XLUMOK events
17766 to 17781	220 nb^{-1}	Problem with two bad AMPLEX cards
16914	$\leq$ 10 nb^{-1}	Not included
17188	$\leq$ 10 nb^{-1}	Not included

Table 15: *Summary of runs excluded from SiCAL 1992 analysis (4.5 % of the integrated luminosity for the two-month running period).*

Finally, using the calculated Bhabha cross-section and the total number of selected events, after background subtraction for the "electroweak run selection" we have :

$$\int \mathcal{L}\ dt = 8749 \pm 10\ \text{(statistical)} \pm 13\ \text{(experimental)} \pm 22\ \text{(theoretical)}\ nb^{-1} \tag{45}$$

Background estimation:		
– Off-momentum particles	(Sect. 6.1)	0.018%
– "Physics" sources	(Sect. 6.2)	0.010%
Trigger efficiency	(Sect. 7.1)	0.010%
Reconstruction efficiency	(Sect. 7.2)	0.001%
Radial fiducial cuts:		
– mechanical precision	(Sect. 7.3)	0.058%
– beam and module alignments	(Sect. 7.4)	0.035%
– modules A-B z-separation	(Sect. 7.4)	0.035%
– asymmetry cuts	(Sect. 7.5.1,2)	0.044%
– shower parametrization and simulation	(Sect. 7.5.3,4,5)	0.023%
Energy cuts	(Sect. 7.6)	0.015%
Acoplanarity cut	(Sect. 7.7)	0.005%
Simulation statistics	(Sect. 8.2)	0.120%
TOTAL experimental uncertainty		0.153%

Table 16: *Summary of luminosity measurement experimental systematic errors.*

10 Conclusion

The overall experimental precision in the 1992 luminosity measurement is estimated to be 0.15 %, limited by Monte Carlo statistics: $0.15\ \% = 0.09\ \%\ exp \oplus 0.12\ \% mc - stat$ and summarized in Table 16. The purely experimental uncertainty is shared between several sources including: thermal expansion of the silicon-detector support ring, uncertainty in the value of the z-separation between the calorimeters, and the fidelity of the Monte Carlo shower parametrization. The theoretical uncertainty is presently evaluated at 0.25 %, dominated by the physical precision of the BHLUMI photon-exchange $\mathcal{O}(\alpha^2)$ leading-log and sub-leading contributions. The background and electroweak corrected SiCAL luminosity cross-section is 84.17 ± 0.10 (statistical) ± 0.21 (theoretical) *nb*. The total integrated luminosity for the 1992 ALEPH-SiCAL electroweak selection is 8749 ± 28 nb^{-1}.

11 Acknowledgements

We express our appreciation particularly to Jacques Lefrancois for many critical discussions and support, as well as to Alain Blondel, Lorenzo Foa, and Dieter Schlatter for their encouragement. We thank Jack Steinberger for the important role he played in getting the SiCAL project started, as well as H. Wahl, G. Pierazzini, C. Cerri and B. Peyaud for their effort during the early stage. We thank Paul Colas and Elizabeth Locci for their help. We would like to thank Bolek Pietrzyk for useful discussions concerning the evaluation of the Bhabha theoretical error.

We would like to express our appreciation to the many collaborators involved in the SiCAL project. In particular, at Saclay we thank L. Gosset and D. Bédérède whose teams designed and built the SiCAL, E. Beuville and J. Pascual who studied front-end and readout electronics; at CERN we thank P. Jarron, G. Stefanini, B. Lofstedt, R. Bennetta, R. Grabit, J. Griffiths and their colleagues who worked on the AMPLEX upgrade and production, front-end readout and the trigger system; at Pisa we thank C. Cerri, C. Avanzini, R. Lorenzini and their colleagues working on the calibration system, the slow-control system and the front-end checkout.

Finally, we thank our laboratories: DAPNIA/CE-Saclay (Direction des Sciences de la Matière, C.E.A.), CERN and INFN Pisa (Dipartimento di Fisica dell'Università, e Scuola Normale Superiore), for their continued support which has made possible both the SiCAL construction and the present analysis.

References

[1] ALEPH collaboration, "A proposal for a low-angle luminosity calorimeter for ALEPH: SiCAL", ALEPH Note 90-8 (CERN/LEPC/90-3).

[2] M. Martinez and J. Rander, ALEPH Note 90-143 (SICAL 90-3).

[3] D. Decamp et al., *Z. Phys.* **C53** (1992) 375.

[4] SiCAL group,"SiCAL - a high precision silicon-tungsten luminosity calorimeter for ALEPH", paper to be submitted to *Nucl. Instru. and Meth.*.

[5] E. Beuville et al., *Nucl. Phys. B* **23A** (1991) 198.

[6] Canberra Semiconductor N.V., Olen, Belgium.

[7] J. Rander and Didier Bederede, ALEPH Note 90-160 (SICAL 90-4).

[8] S.T.C. Societé, Malakoff, France.

[9] H. Hirayama, *Proc. IEEE Nucl. Sci. Symposium*, Orlando, Fla. (1992) 254.

[10] L. Mirabito, *Thesis*, Université d'Aix-Marseille II, France (1991).

[11] F.A. Berends and R. Kleiss, *Nucl. Phys.* **B186** (1981) 22.

[12] S. Kawabata, *Comp. Phys. Comm.* **41** (1986) 127.

[13] J.A.M. Vermasseren, in *Proc. Int. Workshop on $\gamma\gamma$ interactions* (Amiens 1980). Ed. G.Cochard and P.Kessler, Springer-Verlag (1980)

[14] R.D. Field, *Structure functions and total cross sections*, in *Proc. VIII Int. Workshop on $\gamma\gamma$ collisions* (Shoresh, Israel, 1980).

[15] B. Bloch-Devaux and A. Falvard, ALEPH Note 88-197 (Physics 88-56);
S. Dugeay and P. Henrard, ALEPH Note 88-82 (Physics 88-23);
P. Henrard, ALEPH Note 89-25 (Physics 89-7).

[16] G. Barbiellini, B. Borgia, M. Conversi and R. Santonico, *Atti Accad. Naz. Lincei* **44** (1968) 233.

[17] J.F. Crawford, E.B. Hughes, L.H. O'Neill and R.E. Rand, *Nucl. Instru. and Meth.* **127** (1975) 173.

[18] J. Badier, ALEPH Note 87-09 (EMCAL 87-1);
M. Bardadin-Otwinowska et al., ALEPH Note 89-2 (EMCAL 89-1).

[19] W. Beenakker and B. Pietrzyk, *Phys. Lett.* **B296** (1992) 241.

[20] W. Beenakker and B. Pietrzyk, *Phys. Lett.* **B304** (1993) 366.

[21] S. Jadach, E. Richter-Wąs, Z. Wąs and B.F.L. Ward, *Phys. Lett.* **B268** (1991) 253;
S. Jadach, E. Richter-Wąs, Z. Wąs and B.F.L. Ward, *Comput. Phys. Commun.* **70** (1992) 305;
S. Jadach and B.F.L. Ward, *Phys. Rev.* **D40** (1989) 3582.

[22] D.R. Yennie, S.C. Frautschi and H. Suura, *Ann. of Phys.* **13** (1961) 379.

[23] M. Böhm, A. Denner and W. Hollik. *Nucl. Phys.* **B304** (1988) 687;
F.A. Berends, R. Kleiss and W. Hollik. *Nucl. Phys.* **B304** (1988) 712.

[24] W. Beenakker, F.A. Berends and S.C. van der Marck. *Nucl. Phys.* **B349** (1991) 323;
W. Beenakker, F.A. Berends and S.C. van der Marck *Nucl. Phys.* **B355** (1991) 281.

[25] S. Jadach, E. Richter-Wąs, Z. Wąs and B.F.L. Ward, *Phys. Lett.* **B253** (1991) 469.

[26] S. Jadach, E. Richter-Wąs, Z. Wąs and B.F.L. Ward, *Phys. Lett.* **B260** (1991) 438.

[27] H. Burkhardt, F. Jegerlehner, G. Penso and C. Verzegnassi. *Z. Phys.* **C43** (1989) 497.